

---

**LOCALIZED ELECTRON TRAP MODIFICATION AS  
A RESULT OF SPACE WEATHER EXPOSURE IN  
HIGHLY DISORDERED INSULATING MATERIALS**

**Ryan Hoffman, et al.**

**06 March 2017**

**Final Report**

**APPROVED FOR PUBLIC RELEASE; DISTRIBUTION IS UNLIMITED.**



**AIR FORCE RESEARCH LABORATORY  
Space Vehicles Directorate  
3550 Aberdeen Ave SE  
AIR FORCE MATERIEL COMMAND  
KIRTLAND AIR FORCE BASE, NM 87117-5776**

---

## DTIC COPY

### NOTICE AND SIGNATURE PAGE

Using Government drawings, specifications, or other data included in this document for any purpose other than Government procurement does not in any way obligate the U.S. Government. The fact that the Government formulated or supplied the drawings, specifications, or other data does not license the holder or any other person or corporation; or convey any rights or permission to manufacture, use, or sell any patented invention that may relate to them.

This report was cleared for public release by the PRS OPSEC Office and is available to the general public, including foreign nationals. Copies may be obtained from the Defense Technical Information Center (DTIC) (<http://www.dtic.mil>).

AFRL-RV-PS-TR-2017-0064 HAS BEEN REVIEWED AND IS APPROVED FOR PUBLICATION IN ACCORDANCE WITH ASSIGNED DISTRIBUTION STATEMENT.

//SIGNED//

---

Ryan Hoffman  
Program Manager, AFRL/RVBXR

//SIGNED//

---

Dr. Thomas R. Caudill, Acting Chief  
AFRL Battlespace Environment Division

This report is published in the interest of scientific and technical information exchange, and its publication does not constitute the Government's approval or disapproval of its ideas or findings.

# REPORT DOCUMENTATION PAGE

Form Approved  
OMB No. 0704-0188

Public reporting burden for this collection of information is estimated to average 1 hour per response, including the time for reviewing instructions, searching existing data sources, gathering and maintaining the data needed, and completing and reviewing this collection of information. Send comments regarding this burden estimate or any other aspect of this collection of information, including suggestions for reducing this burden to Department of Defense, Washington Headquarters Services, Directorate for Information Operations and Reports (0704-0188), 1215 Jefferson Davis Highway, Suite 1204, Arlington, VA 22202-4302. Respondents should be aware that notwithstanding any other provision of law, no person shall be subject to any penalty for failing to comply with a collection of information if it does not display a currently valid OMB control number. **PLEASE DO NOT RETURN YOUR FORM TO THE ABOVE ADDRESS.**

<b>1. REPORT DATE (DD-MM-YYYY)</b> 06-03-2017		<b>2. REPORT TYPE</b> Final Report		<b>3. DATES COVERED (From - To)</b> 01 Jan 2014 – 30 Sep 2016	
<b>4. TITLE AND SUBTITLE</b> Localized Electron Trap Modification as a Result of Space Weather Exposure in Highly Disordered Insulating Materials				<b>5a. CONTRACT NUMBER</b>	
				<b>5b. GRANT NUMBER</b>	
				<b>5c. PROGRAM ELEMENT NUMBER</b> 61102F	
<b>6. AUTHOR(S)</b> Ryan Hoffmann, Russell Cooper, Daniel Engelhart, Elena Plis, and Dale Ferguson				<b>5d. PROJECT NUMBER</b> 3002	
				<b>5e. TASK NUMBER</b> PPM00018752	
				<b>5f. WORK UNIT NUMBER</b> EF124411	
<b>7. PERFORMING ORGANIZATION NAME(S) AND ADDRESS(ES)</b> Air Force Research Laboratory Space Vehicles Directorate 3550 Aberdeen Avenue SE Kirtland AFB, NM 87117-5776				<b>8. PERFORMING ORGANIZATION REPORT NUMBER</b> AFRL-RV-PS-TR-2017-0064	
<b>9. SPONSORING / MONITORING AGENCY NAME(S) AND ADDRESS(ES)</b>				<b>10. SPONSOR/MONITOR'S ACRONYM(S)</b> AFRL/RVBXR	
				<b>11. SPONSOR/MONITOR'S REPORT NUMBER(S)</b>	
<b>12. DISTRIBUTION / AVAILABILITY STATEMENT</b> Approved for public release; distribution is unlimited. (OPS-17-13147 dtd 27 Mar 2017)					
<b>13. SUPPLEMENTARY NOTES</b>					
<b>14. ABSTRACT</b> The transport of electrons through a highly disordered insulating material (HDIM) is complex and drives our understanding of how spacecraft develop and dissipate potentially damaging electrostatic charge when exposed to the energetic charged particle environment of space. The electrical conduction of spacecraft materials is the prime driver of spacecraft charging. Theories developed to describe doped semiconductors predict that the conduction mechanisms are determined by the distribution and occupancy of electrons in localized electron trap states above the dark current Fermi level. It follows that the density and energy distribution of these trap states plays a key role in the conduction process. However, the density and energy distribution of these traps are not static on orbit and are constantly changing as a result of radiation damage. As a result the electrical conductivity and the optical properties (reflection, absorption, and transmission) are dynamic and cannot be assumed to be the same throughout the mission life of a spacecraft. To elucidate this problem we have undertaken this study to identify the chemically specific damage pathways that result as a consequence of electron bombardment. Here we have shown that radicals formed during electron bombardment play a key role in enhancing the conductivity of polyimide. These radicals are shown to be the likely result of phenol ring rupture in the polyimide monomer. This radiation induced structural change is also observed in the infrared absorption spectrum and the fundamental band gap as shown by UV/VIS transmission spectroscopy. We also show that exposure to air causes these radiation induced morphological changes to rapidly revert to their pre-damaged state. This calls into question the material handling procedures of the last 40 years of similar studies. Polyimide is the prime material under investigation in the study; however, Mylar and low density polyethylene will also be discussed.					
<b>15. SUBJECT TERMS</b> Polyimide, Radiation Damage, Spacecraft, Conductivity, Resistivity, Electron Trap States					
<b>16. SECURITY CLASSIFICATION OF:</b>			<b>17. LIMITATION OF ABSTRACT</b>  SAR	<b>18. NUMBER OF PAGES</b>  42	<b>19a. NAME OF RESPONSIBLE PERSON</b> Ryan Hoffman
<b>a. REPORT</b> Unclassified	<b>b. ABSTRACT</b> Unclassified	<b>c. THIS PAGE</b> Unclassified			<b>19b. TELEPHONE NUMBER (include area code)</b>

This page is intentionally left blank.

# Table of Contents

1.	INTRODUCTION .....	1
2.	BACKGROUND .....	2
2.1	Conductivity.....	2
	Charging (phase I).....	4
	Pre-transit discharge region (phase II).....	5
	Post-transit Discharge Region (phase III).....	5
2.2.	Optical Signature .....	6
2.3.	Material Chemistry .....	7
3.	METHODS, ASSUMPTIONS, AND PROCEDURES.....	8
3.1.	Facilities.....	8
3.2.	Jumbo Space Environment Simulation Chamber .....	9
3.3.	MINION Long Duration Testing Chamber .....	16
4.	EXPERIMENTAL RESULTS AND ANALYSIS .....	17
4.1.	Polyimide .....	17
4.2.	LDPE and Mylar .....	24
5.	CONCLUSIONS .....	25
	SUMMARY OF PUBLICATIONS AND PRESENTATIONS .....	26
	REFERENCES.....	29

## List of Figures and Tables

### Figures

<i>Figure 1 The band structure of a highly disordered insulator with a linear (right) and exponential (left) distribution of trap states. ....</i>	<i>3</i>
<i>Figure 2 Schematic of a charge/discharge curve of an electron irradiated insulating material. ..</i>	<i>4</i>
<i>Figure 3 Schematic of radiation-induced processes in PI.....</i>	<i>7</i>
<i>Figure 4 AFRL at Kirtland Air Force Base in New Mexico. ....</i>	<i>9</i>
<i>Figure 5 Jumbo Environmental Simulation Chamber. ....</i>	<i>9</i>
<i>Figure 6 Interior of the Jumbo Chamber showing the internal instrumentation. ....</i>	<i>10</i>
<i>Figure 7 VUV lamps in JUMBO chamber.....</i>	<i>12</i>
<i>Figure 8 Spectrum of Kr VUV lamps.....</i>	<i>12</i>
<i>Figure 9 Lyman-<math>\alpha</math> intensity falling off as a result of contamination on the lamp window. ....</i>	<i>13</i>
<i>Figure 10 Map of VUV intensity, plotted as equivalent suns, of all three lamps at 22" from the lamp window. ....</i>	<i>13</i>
<i>Figure 11 Electron beam flux at 90keV with rastering as a function of time.....</i>	<i>14</i>
<i>Figure 12 Beam Map of 20keV electrons with rastering.....</i>	<i>14</i>
<i>Figure 13 Beam map of 90 keV rastered electron beam. ....</i>	<i>15</i>
<i>Figure 14 Energy deposited in 76 <math>\mu</math>m Kapton by 90 keV electron beam. ....</i>	<i>15</i>
<i>Figure 15 Front panel of LabVIEW automated control program. ....</i>	<i>16</i>
<i>Figure 16 Charge and discharge curves for three identical samples of PI mounted at different positions on the sample wheel.....</i>	<i>16</i>
<i>Figure 17 The exterior and interior of MINION chamber .....</i>	<i>16</i>
<i>Figure 18 Transmittance spectra of reference (pristine) PI film and radiation damaged PI at different doses. ....</i>	<i>18</i>
<i>Figure 19 Change of fundamental bandgap of radiation-damaged PI at different GEO dose equivalents. ....</i>	<i>18</i>
<i>Figure 20 Transmittance spectra of radiation-damaged PI with <math>5.6 \times 10^7</math> Gy dose measured after (20-260) min of air exposure. ....</i>	<i>18</i>

*Figure 21 Absorbance spectra of pristine and electron radiation-damaged PI after 20 min of air exposure. .... 19*

*Figure 22 Top – difference spectrum of radiation-damaged and pristine PI material. Bottom – the 2<sup>nd</sup> derivative of difference spectrum.. .... 19*

*Figure 23 Intensity of selected absorption bands of radiation damaged PI with  $5.6 \times 10^7$  Gy dose as a function of air exposure time..... 20*

*Figure 24 Normalized surface potential versus time..... 20*

*Figure 25 Selected parameters ( $\mu_0$  (mobility),  $r_r$  (release probability), and  $r_t$  (trapping probability)) obtained from fitting of Eq. (4) to the surface potential discharge curves as a function of vacuum exposure..... 21*

*Figure 26 Radical concentration of radiation-damaged Kapton with a dose of  $4.0 \times 10^7$  Gy as a function of vacuum exposure. .... 21*

*Figure 27 Comparison of air- and vacuum-recovered conductivities of Kapton irradiated with electron dose of  $5.6 \times 10^7$  Gy..... 21*

*Figure 28 Conductivity of radiation-damaged Kapton with electron dose of  $5.6 \times 10^7$  Gy as a function of vacuum exposure. .... 21*

*Figure 29 Resistivity (inverse of conductivity) and EPR signal of radiation damaged PI film plotted as a function of cumulative air exposure time ..... 22*

*Figure 30 XPS results on PI as a function of dose. .... 23*

## Tables

*Table 1 Publications ..... 26*

*Table 2 Presentations ..... 28*

This page is intentionally left blank.

# 1. INTRODUCTION

Exposure of spacecraft to the energetic charged particle environment of space leads to material degradation, or aging. Our knowledge of how a spacecraft material behaves is based almost solely on its pristine material properties and does not take into account the fact that these materials age continuously when on orbit. This poor understanding leads to decreased satellite lifetime, poor space situational awareness (SSA), poor anomaly resolution and decreased system reliability. Highly disordered insulating materials (HDIMs) like polyimide (PI, Kapton®) and polytetrafluoroethylene (PTFE, Teflon®), are commonly used in the spacecraft industry for their insulating properties, mechanical durability, low density and resistance to radiation and atomic oxygen damage. These desirable properties are largely an outgrowth of the exceptional chemical stability of these polymers. However, damaging radiation fundamentally changes these materials, leading to dynamically changing properties that must be understood in order to properly model and predict spacecraft behavior.

Material aging in space is caused by energetic particles or photons bombarding the spacecraft surface. The particle primarily responsible for damage is dependent on the orbit. In low Earth orbit (LEO) the primary damage source is atomic oxygen (AO) and research has been focused on surface degradation [1-5], the materials' mechanical property changes [6-8], and volatile reaction products. [9] This research led to the development of AO resistant materials and protective coatings to help mitigate the damage. [10-15] Exposure of dielectric materials to high energy electrons, like those present at geosynchronous Earth orbit (GEO), causes changes in their electrical and optical properties, in particular conductivity [16-19] and optical absorptivity. [20-22] Since GEO electrons are fairly high energy (10's of keV to MeV) the aging is not limited to the surface of the material, but is also acting on the bulk. It is in this orbital regime that we have focused our studies.

Of particular importance is the alteration of electrical conductivity in aged HDIMs as a result of exposure to high energy particles. This effect cannot be overstated; conductivity defines space charge accumulation and subsequent electrostatic discharge, leading to insulating material degradation and premature material failure. Numerous reports provide an essential background to general charge transport [23-26], but they fail to address the chemical aging mechanisms seen on orbit. What is clear is that conduction mechanisms will evolve due to exposure to extreme environments [27, 28], however, the extent and chemical mode of this change has not been adequately addressed.

Generally, space radiation induced charging of HDIMs is determined by the interplay between two key fundamental processes; the charging of the material from electron, photon, and ion bombardment, and the discharging of the material via generation of secondary electrons and a material's ability to transport that charge within the material. [29] When immersed in the space environment, HDIMs obtain a net charge that is a function of the charging rate and the discharging rate. These rates are dependent on the details of the material's band-gap and the space charge trap density or density of states (DOS) that exist within that gap. [30, 31] This process is analogous to conduction in doped semiconductors, where the conduction mechanisms are determined by the distribution and occupancy of electrons in localized electron trap states above the dark current Fermi level. Theory developed to describe charge conduction in doped semiconductors provides a basic theoretical framework to understand the role of DOS in HDIMs' conduction [32, 33]. It

follows that the density and energy distribution of space charge trap states plays a key role in the conduction process. However, models adapted from semiconductor physics to describe the behavior of HDIMs assume a static DOS and do not address the issue of state modification as the material ages.

This work is an investigation into the chemical changes that occur in HDIM materials when exposed to simulated GEO electron environments and the relation of these chemical changes to charge transport. In particular, we seek to gain a comprehensive knowledge about the nature of the trap states in HDIMs and the chemical and morphological structures that give rise to them. Several complementary characterization techniques will be utilized to qualify and quantify radiation induced chemical changes in the material. Relating the chemical changes of aged materials to alterations of charge transport will give insight into the nature of charge transport itself and help guide the design of novel technology-enabling materials.

## **2. BACKGROUND**

This work seeks to understand the two material parameters that are key to our understanding of the material lifecycle and its impact on spacecraft design. The two properties that we focus on are the electrical conduction and the optical signature (reflectivity, absorption and transmission). These two seemingly disparate properties are both fundamentally related to the DOS within the bandgap of the material. We also discuss some chemical structures within the material that give rise to the defect states that develop in the material during electron bombardment.

### **2.1 Conductivity**

When exposed to the space environment, HDIMs obtain a net charge due to electron/ion bombardment or photon irradiation. The rate at which this charge builds up is a function of the interplay between charge capture and the transport of that charge through the material to the spacecraft chassis.[34] Charge transport depends on the trap DOS that exists within the materials' band gap.[30, 35] Models developed to describe disordered semiconductors have proven effective in describing DOS effects in electron transport through narrow band-gap materials. These models, however, assume a static DOS and do not address the issue of state modification as the material ages.[36-38] Though useful, terms borrowed from solid-state physics such as band gap, valence and conduction band, etc. are not strictly correct as HDIMs lack a true unit cell.

As materials are bombarded with high energy radiation, energy is shared with many bound (valence) electrons within the material, which can be excited into energy levels in the conduction band (black dots in Figure 1), thereby facilitating their mobility. The conductivity of the material is therefore enhanced by the radiation energy. This conduction mechanism is known as radiation induced conductivity (RIC).[39] These excited electrons provide a significant conduction mechanism in HDIMs exposed to high energy radiation, but the electrons quickly thermalize to shallow localized trap states just below the conduction band edge (red dots in Figure 1). Theory predicts that the conduction mechanisms are determined by the distribution and occupancy of these electrons in localized trap states above the dark current Fermi level.[40]

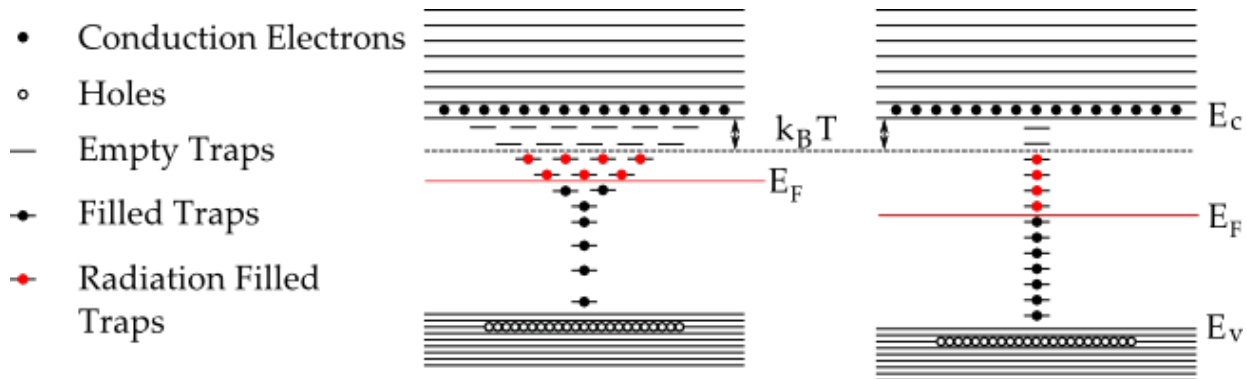


Figure 1 The band structure of a highly disordered insulator with a linear (right) and exponential (left) distribution of trap states.  $E_c$  is the bottom of the conduction band,  $E_v$  is the top of the valence band,  $E_F$  is the Fermi level. Traps below  $E_F$  are shown as full because they are active in non-RIC conduction.  $k_B T$  are the shallow trap states where electrons can be thermalized into the conduction band.

Similar to radiation-induced conductivity of semiconductor materials, a flux of penetrating electrons in these shallow traps can: (i) remain in these shallow trap states; (ii) be thermally re-excited into the conduction band, leading to thermally assisted charge transport, termed radiation induced conductivity (RIC) [41]; (iii) decay into deep traps well within the band gap, often accompanied by photon emission which is termed cathodoluminescence; (iv) hop to an adjacent trap, termed thermally assisted hopping conductivity or dark current (DC) conductivity [42]; or (v) decay to low level valence band or trap states through radiative or non-radiative processes termed recombination [43]. The occupancy of these states depends on the number of electrons that can potentially populate the states, the number of states that can be populated, and the trapping and retention rates of the states. This simple conduction model does not take into account the generation and/or destruction of traps as the material ages. While it is known that the conduction mechanisms will evolve with radiation damage [27], the extent and chemical nature of that evolution has not been determined.

Since the trapping and release of stored electrons is determined by the density and distribution of trap states it is possible to probe the material by charging it with an electron beam and monitoring the surface potential as it decays to 0 V.[44-46] A schematic of the surface potential which develops on HDIM during and after electron bombardment is shown in Figure 2. The charging phase (region I) starts with material mounted on a grounded back plate being exposed to a known non-penetrating electron flux and the resultant potential being measured with a non-contact electrostatic voltmeter. Since the electron beam is low flux and the electrons are low energy and therefore have a much shallower maximum penetration depth, this process will not age the material significantly.

This process is continued until an equilibrium surface potential is reached or the voltage is  $\sim 80\%$  of the material's breakdown potential. During this phase the surface potential is dictated by the balance of secondary electron (SE) yield, the trap DOS and dark current (DC) conduction. The discharge phase begins when the electron beam is extinguished and the embedded charge flows through to material and slowly bleeds away to ground. This process is monitored by measuring the surface potential of the material in vacuum.

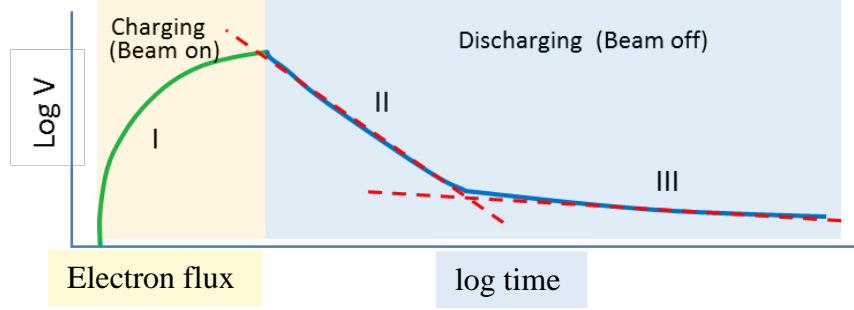


Figure 2 Schematic of a charge/discharge curve of an electron irradiated insulating material. Three regions correspond to (I) charging section dependent on the balance of electron capture, secondary electron generation, DOS and DC conductivity. Discharge section is broken into the pre and post transit, with dashed lines added to guide the eye. (II) pre-transit discharge section, (III) post-transit discharge section with dominating dark current conduction.

The discharge phase features two distinct parts (regions II and III in Figure 2). The surface potential in region II is driven by the complex redistribution of charge within the bulk of the material, but there is no net loss of charge as the deposited charge body has not traversed the material. This is the pre-transit portion of the discharge. Region III begins when the lead edge of the charge body reaches the grounded back plate and is removed from the material. The change in surface potential during this post-transit section is a function of electrons leaving the system to ground via DC conductivity.

Models developed over the past several decades enable the extraction of many material parameters from a charge/discharge curve, including the density of trapped states (region I), trapping and de-trapping rates and effective electron mobility (region II), and dark resistivity and conductivity of the material (region III). Due to the complex nature of charge-discharge curve, its each region is fitted independently, as described below.[31, 32, 41, 46-51]

### Charging (phase I)

To model the surface charge during the charge up process of electron-irradiated HDMI, the charging model developed by A. Sim [31] may be used:

$$V_s(t) = \frac{q_e d N_t}{\epsilon_0 \epsilon_r} \left\{ 1 - \frac{R(\epsilon_b)}{d} \right\} R(\epsilon_b) \left[ 1 - \exp \left\{ \frac{S_c J_b \tau_{onset} (1 - \sigma_{yield})}{q_e (1 - m)} \right\} \left[ 1 - \left( 1 + \frac{t}{\tau_{onset}} \right)^{1-m} \right] \right] \quad (1)$$

Here  $q_e = 1.602 \times 10^{-19}$  C is the charge of an electron;  $\epsilon_0$  and  $\epsilon_r$  are the permittivity of free space and relative permittivity of the LDPE material, respectively;  $J_b$  is a beam flux, nA/cm<sup>2</sup>;  $d$  is a sample thickness. The yield,  $\sigma_{yield}$ , may be estimated based on the measurements and models of Song *et al* for a 20 keV incident electron beam.[52, 53] For LDPE, the  $\sigma_{yield}$  equals 0.3 emitted

electrons per incident electron. The range  $R(\epsilon_b)$  is a maximum distance that an electron of a given incident energy can penetrate through the material before all kinetic energy is lost and the electron comes to rest. For LDPE  $R(\epsilon_b)$  was estimated to be 8.3  $\mu\text{m}$ .

## Pre-transit discharge region (phase II)

The Toomer and Lewis model (eq. 2) is utilized to describe the conduction process in HDIM in this phase.[54] Assuming the instantaneous charge injection conditions with no surface traps, this correspond to two decay processes  $\alpha_1 = 0$ , and  $\alpha_2 = \infty$ , it may be reduced to the simpler expression (eq. 3).

$$V(t) - V_0 = \frac{-\mu_0}{2R} \left(\frac{V_0}{d}\right)^2 \int_0^t (r_r + r_t e^{-Rt}) \left[ 1 - \left( \sum_{n=1}^{\infty} a_n e^{-\alpha_n t} \right)^2 \right] dt \quad (2)$$

$$\frac{V(t)}{V_0} = 1 - \frac{V_0 \mu_0}{2d^2 R} \left( r_t t + \frac{r_t}{R} \{1 - e^{-Rt}\} \right) \quad (3)$$

With no dispersive parameter taken into account and no active surface traps presented, a fitting based on eq. (3) predicts only the first several seconds of the pre-transit discharge. To model the entire fast discharge region (0.1-100 sec), eq. (3) needs to be integrated using the non-zero dispersive term  $\lambda$  to account for the highly disordered HDIM structure. In addition, we assumed that a fraction,  $a_1$ , of the charge is initially placed on the surface traps, from where they move to the bulk at a certain rate  $\alpha$ . The rest of the charge ( $1-a_1$ ) is injected directly into the bulk immediately after the discharge. Then the surface potential of the charged sample decays as

$$\begin{aligned} \frac{V(t)}{V_0} = & 1 - \frac{V_0 \mu_0}{2d^2 R} \left( r_t t + \frac{r_t}{R} \{1 - e^{-Rt}\} + \frac{r_r a_1^2}{2\alpha} \{1 - e^{-2\alpha t}\} \right) \\ & - \frac{V_0 \mu_0}{2d^2 R} \left( \frac{r_t a_1^2}{R + 2\alpha} \{1 - e^{-(R+2\alpha)t}\} \right) - \lambda t^\beta \end{aligned} \quad (4)$$

Where  $R = r_r + r_t$ ;  $r_r$  and  $r_t$  are probabilities of charge per unit time to be released from the trap and to be re-trapped in different trapping center, respectively;  $d$  is the thickness of the sample and  $\mu_0$  is the mobility of the carriers in HDIM material between traps. The initial values of free parameters  $r_r$ ,  $r_t$ ,  $a$ ,  $\alpha$ , and  $\beta$  are estimated from the literature to provide a starting point for the fit.

## Post-transit Discharge Region (phase III)

After the front of the charge body has reached the grounded backplane, the dissipation of charge is primarily determined by the loss of electrons from the material. Treating a thin film insulator as a simple capacitor, the charge decay time is proportional to resistivity. As a first approximation, the thin-film insulator can be treated as a planar capacitor (with the charged front surface and conducting rear electrode acting as the electrodes), which discharges in an Ohmic fashion through

the bulk of the insulator to the grounded back plane. In this approximation, the RC-time constant or relaxation time,  $\tau$ , for discharging insulator can be written as:

$$\rho = \frac{\tau}{\epsilon_r \epsilon_0} \quad (5)$$

where  $\rho$  is the material resistivity, and  $\epsilon_0$  is the permittivity of free space. The relative dielectric constant,  $\epsilon_r$ , of nearly all spacecraft insulators lie within a narrow range, 2-5, and is well known for most materials; thus, determination of the resistivity follows directly from measuring the relaxation time. Therefore,  $\tau$  is equivalently the relaxation time or the charge storage decay time, i.e. the time it takes for the surface charge to drop to 1/e of its initial value. Note that in this simple model, decay time is an intrinsic material property independent of surface area or thickness.

To determine  $\tau$  one needs only find the time when the surface potential reaches 1/e of its initial value. Because we have assumed a discharging capacitor model it is most consistent to use the ordinary differential equation for voltage as a function of time  $\frac{dV}{dt} = -\frac{1}{RC}V$  which has the solution  $V(t) = V_0 e^{-t/RC}$  where  $RC = \tau$ ,  $V_0$  is the initial voltage and  $t$  is time.

## 2.2. Optical Signature

In the visible and ultraviolet bands, the main electromagnetic absorption process in dielectrics originates from the interaction of light with electrons.[55-57] If the incident photon has a frequency such that its energy matches the energy needed to excite an electron to a higher energy state, then the photon may be absorbed. The electron may be an ion-core electron or a free electron in the solid. If the energy of the incoming photon does not match the required excitation energy, no excitation occurs and the material is transparent to such radiation. In nonmetal solids such as polyimide, there is a minimum energy separating the highest filled electron states (valence band) and the lowest empty ones (conduction band). Electron transitions from band to band constitute the strongest source of absorption. In dielectrics, such as glass, quartz, some salts, diamond, many metal oxides, and most plastic materials, no excitation resonances exist in the visible spectrum. However, this is not the case for polyimide with a band gap of  $\sim 2.5$  eV, well within the visible range. This is what gives polyimide its distinctive orange color.

The situation just depicted is ideal in the sense that we have considered a *perfect* dielectric material. All dielectrics have some degree of disorder ranging from semi-crystalline low density polyethylene to fully disordered polyimide. This disorder gives rise to a large density of localized electron trap states at energies between the valence and conduction bands. These localized electron states are a source of absorption; that is, electrons are excited from the valence band to localized states and/or from them to the conduction band. In all cases, the absorption due to defects is less than that of the fundamental band edges, but defect-dependent absorption does affect the optical properties in a non-negligible way.

UV/Visible absorption spectroscopy may be used to evaluate the change in the fundamental bandgap of irradiated polyimides. Moreover, UV/visible transmission measurements can be used to study the composition, color, and, most importantly for these studies, the radiation-induced defects in a material. Fourier transform infrared (FTIR) spectroscopy probes chemical bonding by exciting vibrational transitions within the molecule. Because every chemical bond has unique

vibrational energy states, measuring which wavelengths of IR light are absorbed provides highly specific chemical information. This technique provides information on the molecular bonding environment, chain conformation, and orientation of specific functional groups of pristine, damaged, and recovered PIs. Changes in the position and intensity of the IR absorption “fingerprint” of damaged and recovered materials offer further insights into what chemical bonds are being modified during the radiation-induced degradation and recovery process.

### 2.3. Material Chemistry

A fundamental understanding of the structure of the bandgap in dielectric materials is critical to predicting their response to ionizing radiation, but does not help to mitigate unwanted responses and develop the next generation of materials. For this we need to know what chemical structures give rise to the localized electron trap states.

Exposure of dielectrics to a simulated space environment will change its chemical structure. The nature and extent of this change is a function of several simultaneous kinetic processes, namely, damage (interaction of PI with highly energetic particles, resulting in broken chemical bonds), healing (formation of bonds identical to those damaged, returning the material to its pristine state), and scarring (formation of new chemical bonds in damaged material which are different from those in the pristine material). In order to understand and predict properties of a spacecraft material as a function of time spent in a particular orbit, the processes of damage, healing, and scarring must be understood individually as depicted in Figure 3.

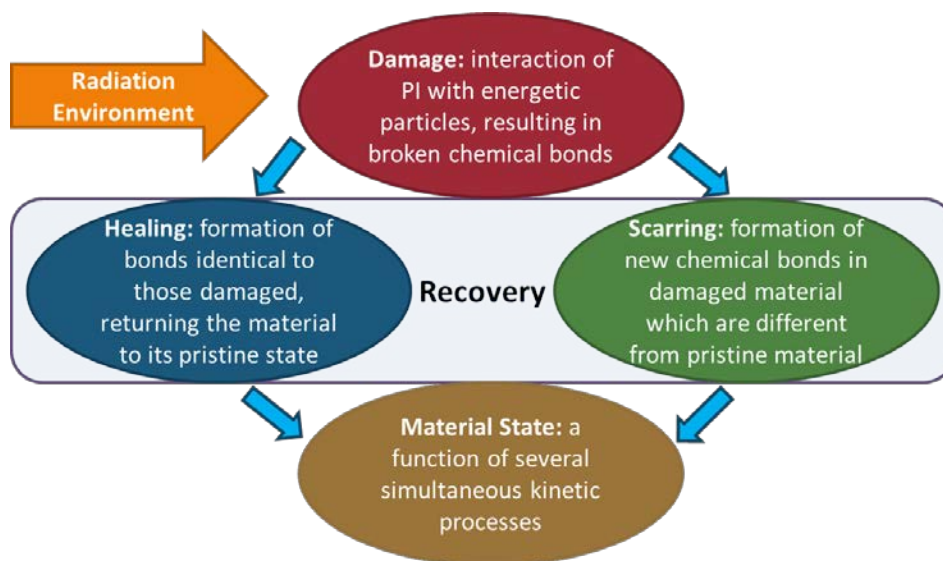


Figure 3 Schematic of radiation-induced processes in PI.

Probing the fundamental nature of electronic conduction in HDIM can be accomplished via a suite of materials characterization techniques. X-ray photoelectron spectroscopy (XPS) can be used to measure the elemental composition and chemical and electronic states of the elements that exist in a material. Nuclear magnetic resonance (NMR) uses an effect by which unpaired protons or neutrons in atomic nuclei absorb and re-emit electromagnetic radiation. The energy of these transitions is dependent on the strength of an applied magnetic field and the magnetic properties

of the atoms under investigation. By studying changes in the absorption/emission wavelength of known isotopes of well-studied atoms (chemical shift), information can be gleaned about the bonding environment of different atoms within the structure. Electron paramagnetic resonance (EPR) is analogous to NMR, but measures the perturbations in an applied magnetic field brought about by unpaired electrons. These material investigation techniques, coupled with the spectroscopy detailed above, offer extremely detailed insight in the chemical structure, especially when delineating changes between pristine and aged materials.

Analogous to defects in a periodic lattice, electron trap states can be usefully thought of as deformations of a homogenous disordered polymer structure that give rise to an energetic distribution of electronic states whose energy falls within the band gap of the material. These intermediate energy states facilitate electronic conduction by defining allowed electronic transitions either from the top of the conduction band or the bottom of the valence band which are less energetic than the material's band gap. A change in the number and energetic distribution of these defect states can be reasonably expected to manifest as a change in the material's bulk conductivity. By characterizing pristine and aged materials under space-like conditions and correlating this chemical information to the changes in bulk physical properties, the fundamental mechanisms of charge conduction may be hypothesized. A detailed understanding of charge transport in individual materials will lead to generalized theory of conductivity and enable the design of new technology enabling materials.

### **3. METHODS, ASSUMPTIONS, AND PROCEDURES**

#### **3.1. Facilities**

There are two main test facilities in Spacecraft Charging and Instrument Calibration Laboratory (SCICL) that have been adapted to facilitate this work, the Jumbo chamber and the MINiature ION chamber (MINION). Jumbo is the largest chamber and has been fitted with electron, ion and photon sources that have been designed to simulate aspects the space environment. All materials were aged in Jumbo and much of the characterization was also done in this chamber. In the last year of this project we discovered that many of the tests we wanted to perform required months of time in the vacuum chamber. A high level of automation was implemented to reduce the number of man hours required, but these test were still occupying our primary research facility for much too long. To overcome this the MINION chamber was brought online to allow long-duration tests without disruption of work flow. Both chambers will be described below.

### 3.2. Jumbo Space Environment Simulation Chamber

The Jumbo vacuum chamber is a 1.8m x 1.8m cylindrical chamber and resides within SCICL in the Space Vehicles Directorate of AFRL at Kirtland AFB (see Fig. 4). It has 20 ISO and Conflat (CF) ports ranging from 2.75” to 22” and a bevy of mechanical, gas and electrical feedthroughs. Jumbo is a completely dry-pumped chamber allowing minimal surface contamination of test materials. The chamber is primarily pumped with a two stage Sumitomo Marathon CP-20 cryo-pump operating at 13 K. The cryo-pump has a 20” aperture and a pumping speed of 582,000 L/min. It can take the chamber from rough vacuum ( $10^{-3}$  torr) to high vacuum ( $10^{-6}$  torr) in fifteen minutes. The cryo-pump is backed with an Alcatel ACG 600 which consists of a dry multi-stage roots pump and a roots blower, with a peak pumping speed of 8000 L/min. The ACG 600 can rough pump the chamber from atmosphere to rough vacuum ( $10^{-3}$  torr) in thirty minutes. There is an additional oil-free 18” Mitsubishi FT3301W turbo-molecular pump, 360,000 L/min, that is backed with a 600 L/min Varian tri-scroll dry pump. The Turbo pump, operating on its own, can bring the chamber to high vacuum in several hours, but is primarily used when gas is flowing into the chamber to avoid saturation of the cryo-pump. Jumbo contains a thermal stage that can be cooled to liquid nitrogen ( $LN_2$ ) temperatures and heated to 80°C and is used as a sample mounting plate. For typical operations the stage is held perpendicular to the incident beams; however it can be swiveled to provide grazing incident angles. While not currently in operation, the stage can be used in conjunction with a  $LN_2$  cryo-shroud to provide a 360° simulated “cold view-to-space”.



*Figure 4 AFRL at Kirtland Air Force Base in New Mexico.*



*Figure 5 Jumbo Environmental Simulation Chamber.*

Figure 6 shows the interior of the Jumbo chamber with internal instrumentation. Jumbo is equipped with four automated motion stages used for a variety of measurements. A three axis translational stage provides a moveable platform for various sensors and sample holders in Jumbo. These stages are automated with Phytron rad-hard stepper motors capable of controlling the location of any attached probes or samples with sub-millimeter resolution. Three of the stages are linear; two with a 24” range of travel and the third with 18”. The fourth stage is rotational with 0.4° resolution and is used with a sample mounting wheel to rotate materials within the beam to normalize exposure. This system allows the sample carousel and probes to be moved closer to the location of the

electron, ion and VUV sources. This allows some degree of control over the beam size and flux of each of the sources by taking advantage of geometric factors, and will be discussed in greater detail later in the section covering the Jumbo's source capabilities.

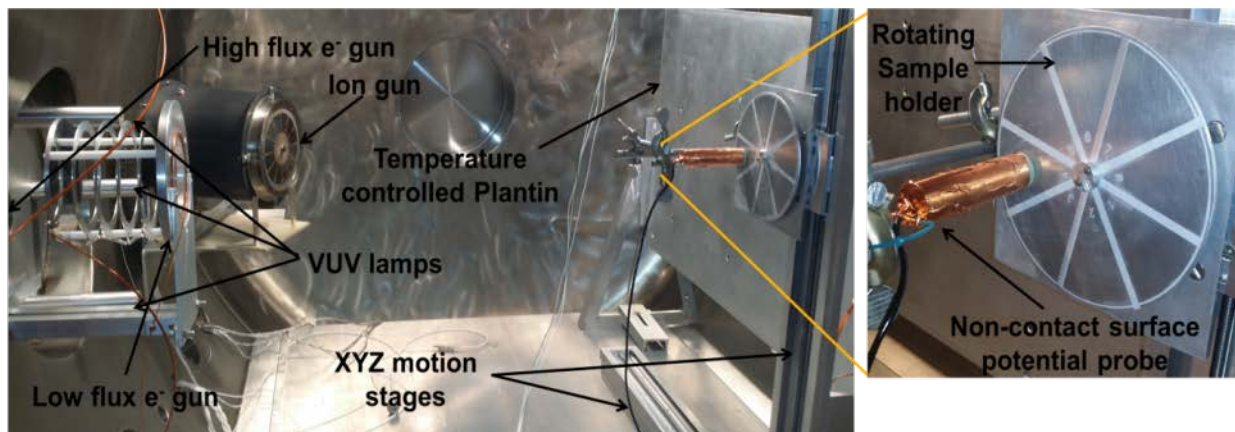


*Figure 6 Interior of the Jumbo Chamber showing the internal instrumentation.*

The rotatable sample carousel is capable of holding eight different sample test coupons. However, one position is typically left empty to provide a control. Mounting multiple samples allows an increased testing rate and increases the consistency of the measurements made on each sample. The rotation of the wheel plays three important roles. First, all samples are exposed to the same portions of the electron, ion, or VUV beams ensuring each sample has been exposed to the same environment. Second, rotating the materials through the beam insures uniform exposure by averaging out spatially varying beam profiles. Third, instead of bringing a surface voltage probe in periodically to measure the samples, we can constantly measure the surface potential of the samples as they are exposed. The carousel platform has the capacity to hold any of the diagnostic probes such as Faraday cups or Langmuir probes needed to monitor conditions during the test. The platform can be mounted anywhere in the chamber, however it is most often mounted to the 3-axis stage for greater flexibility.

Jumbo contains several standard vacuum probes. There are ion and convectron gauges to measure the pressure in the chamber. We utilize the ion gauge as a vacuum interlock for both our electron gun and our non-contact surface probe. Jumbo also has a Stanford Research Systems RGA-300 residual gas analyzer used to identify vacuum contamination and leaks in the chamber and a quartz crystal microbalance (QCM) is also available for precise cleanliness evaluation. Jumbo is also equipped with a variety of specialized probes that are used to quantify our various sources and to probe the surface voltage of the materials under investigation.

Jumbo has two Faraday cups. The first is a Kimball Physics model FC-71A used to monitor fluxes from the Kimball Physics electron gun. It has a  $0.5 \text{ cm}^2$  aperture area and a retarding grid capable of 1000V in order to identify beam energy. We can both put voltage on the retarding grid and read the current output of the Faraday cup with a Keithley model 6487 source/meter. The Keithley meter has a detection limit 0.01 pA. However, our ammeter and Faraday cup system is limited by the noise introduced from the Faraday cup cabling and the BNC feedthroughs on the chamber.

These factors limit current detection resolution to  $0.2 \text{ pA/cm}^2$ . This resolution is well below the normal fluxes we use in experiments and does not create much error in our measurement.

The second Faraday cup is a planar Faraday probe with a  $0.5 \text{ cm}^2$  collection plate capable of being biased to  $\pm 500\text{V}$  manufactured by Plasma Controls LLC. This probe allows for easy electron or charged species measurements. Positive bias results in rejection of positively charged ions and negative bias rejects negatively charged particles. This probe, in conjunction with a Langmuir probe, provides excellent plasma characterization.

Jumbo is equipped with a spherical Langmuir probe capable of measuring plasma potential, plasma density, and electron temperature of Jumbo's plasma source. It is a standard  $3.175 \text{ cm}$  diameter Langmuir probe manufactured by Plasma Controls LLC. A Keithley 2410 high voltage source/meter is used to bias the probe and simultaneously record the current. This system uses the pulse sweep technique of measuring the electron temperature and density and is far less sensitive to surface contamination than traditional sweep methods.

There are two different non-contact surface potential probes for Jumbo. Both probes are produced by Trek Inc. Trek probe model 370 is capable of  $-3$  to  $3\text{kV}$  and has an extremely fast,  $50\mu\text{s/kV}$  response to changing surface potentials. Trek probe 341B is capable of  $-20$  to  $20\text{kV}$  with a  $200 \mu\text{s/kV}$  response time. During our charging experiments the probe sits over a stationary sample for at least one second before taking the measurement, ensuring that both of our probes have more than sufficient time to measure accurately. These probes are critical to our experiments as they can accurately measure the surface potential without bleeding any of the charge away. The difficulty in using a non-contact probe is that the material-to-probe distance is critical. The probes must be  $3 \text{ mm} \pm 1 \text{ mm}$  away from the samples. Mounting the sample carousel so that when rotated the sample/probe distance is constant during rotation can be challenging. The *in situ* cabling was placed in Teflon tubing to prevent arcing from the cabling and both the probe holder and tube were wrapped in Cu tape to prevent them from charging. Any charging on the insulators surrounding the probe or the cabling results in erroneous readings from the non-contact probe and consequently must be avoided.

The energetic particle space environment is a complex and dynamic environment that can range in energy and flux over many orders of magnitude. For this reason it is impossible to simulate all aspects simultaneously and tradeoffs must be made to arrive at a practical system. We have focused on the electron and photon environment of GEO and the electron, photon and ion environment of LEO.

In GEO the light most likely to damage polymer materials is the Lyman- $\alpha$  line of hydrogen at  $121.6\text{nm}$ . This vacuum ultraviolet (VUV) light has enough energy ( $\sim 10 \text{ eV}$ ) to break most chemical bonds in polymer materials. This is also the region of the solar spectrum most responsible for generating photoelectrons as these photons have energy greater than the band gap of most insulators. In order to mimic Lyman- $\alpha$  line of hydrogen, four Krypton lamps were acquired from Resonance Ltd. Krypton. Three of these lamps are mounted on  $2 \frac{3}{4}$  inch CF flanges in a circle around our high energy electron gun and perpendicular to the chamber axis and sample stage (see Fig. 7). With transitions at  $123.6 \text{ nm}$  and  $116.5 \text{ nm}$ , Fig. 8, they are an excellent approximation for the Lyman- $\alpha$  line.



Figure 7 VUV lamps in JUMBO chamber.

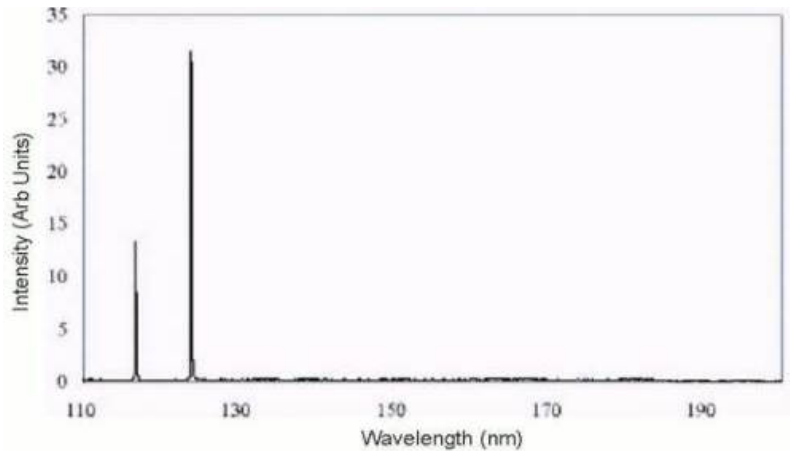


Figure 8 Spectrum of Kr VUV lamps.

These lamps are six inches from the center of the electron gun. A Hamamatsu phototube R1187 is used to measure the output of the VUV lamps using a Keithley model 6487 picoammeter. To map the uniformity of the spot, the photocathode was mounted on the three-axis translational stage and raster scanned over the range of the stages. The three lamps have nearly identical divergence of  $40^\circ$  FWHM; however they produce different VUV fluxes. The VUV flux is highly dependent on the cleanliness of the windows on the VUV lamps. Due to background contamination in the chamber, especially silicones, a thin residue forms on the windows when they are in use in the chamber. The Jumbo chamber is quite clean and all effort is made to minimize the contamination.

The solar flux of Lyman- $\alpha$  light is variable in GEO orbit, but the average baseline for photon flux is  $2.5 \times 10^{11}$  photons/cm<sup>2</sup>/sec.[58] We calculate the equivalent suns (acceleration factor) of our lamps by dividing our photon flux by the literature GEO flux mentioned above. Equivalent suns at Lyman- $\alpha$  line produced by three Krypton lamps is plotted as a function of time in Fig. 9. The lamps were cleaned well and then the chamber was pumped down for three days before these data were collected.

When using the VUV lamps, we clean them each time with aluminum oxide powder; however over the course of time (tens of hours) the total output of the lamp drops. Because the formation of this thin residue is proportional to the constant vacuum level it is easy to correct for this drop in VUV output by monitoring the VUV photocathode during lamp usage. We discussed this decrease with the manufacturer of the lamps and they noted that the decrease in output flux we see is smaller than they expect, indicating the cleanliness of our vacuum.

We are not able to control the divergence of the VUV lamps; however we can move the sample wheel in order to adjust the size of the beam and maximize the exposure of the samples to the VUV lamps in order to increase the VUV aging factor.

The map in Fig. 10 corresponds to the closest the sample holder can be placed to the VUV lamps with the 3 axis stages. The VUV lamps give a very uniform beam and the small amount of asymmetry in the VUV beam is due to the difference in flux from the different lamps. With these

fluxes in mind and knowing the approximate VUV decrease due to contamination of the VUV window we are able to expose our samples to  $> 10x$  GEO fluxes. This is the maximum from the VUV lamps, and we can control the RF field in order to decrease the VUV output in a controlled fashion.

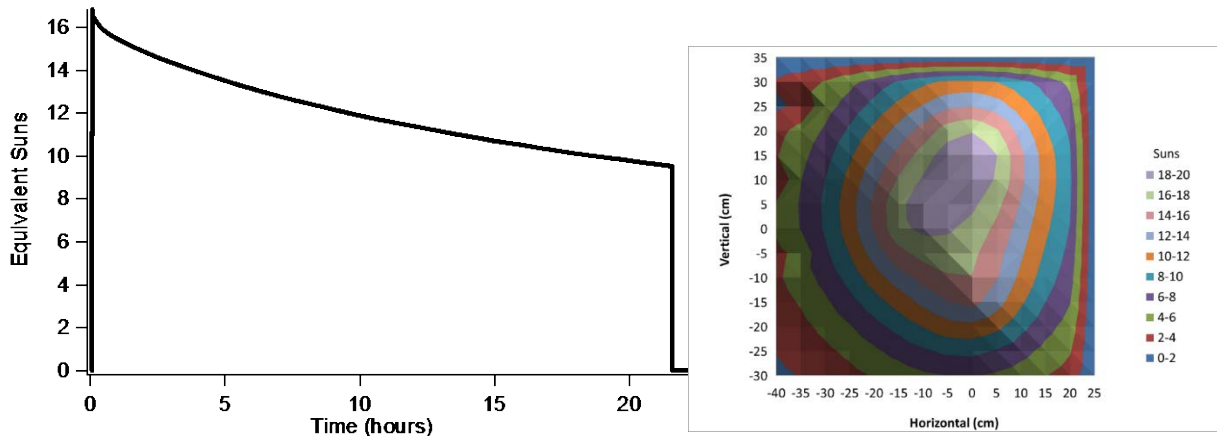


Figure 9 Lyman- $\alpha$  intensity falling off as a result of contamination on the lamp window.

Figure 10 Map of VUV intensity, plotted as equivalent suns, of all three lamps at 22" from the lamp window.

The primary electron source in Jumbo is a Kimball Physics EG8105-UD electron flood gun with a range of 1keV-100keV. This gun has two main purposes. First, a 20 keV beam acts as a charging source by injecting shallow penetration ( $\sim 5 \mu\text{m}$ ) electrons into thin ( $25\text{-}75 \mu\text{m}$ ) test materials. The flux of the electron gun is controllable from  $\text{pA}/\text{cm}^2$  to tens of  $\text{nA}/\text{cm}^2$ . Low fluxes ( $50 \text{ pA}/\text{cm}^2$ ) of 20keV electrons are used to simulate a flux that might be seen in GEO.[59] The electron flux does vary  $\sim 30\%$ , especially after it is initially turned on, but this is overcome by allowing the gun to warm up for several hours before making any measurements. Typical flux stability is shown in Fig 11. This flux is in the range that materials would be exposed to in space in GEO. These fluxes also charge the samples at a rate that allows the materials to reach equilibrium in several hours, a time frame that allows us to capture the subtleties of the charging and to derive the underlying physics. The electron beam as it comes out of the gun at 20 keV without focusing has a low divergence of  $< 5^\circ$ . This requires a rastering of the electron gun in order to create a broader electron beam to provide a uniform exposure of the materials under investigation. Rastering is a systematic perturbation of the electron beam angle by use of electromagnets to steer the beam in two dimensions. Appropriate raster settings to create a uniform beam of the appropriate size must be experimentally determined for each electron beam energy. It is important that the raster scan take place on a fast time scale relative to the sample rotation to ensure that there is no aliasing of the electron beam on the rotating sample holder leading to a non-uniform exposure. The maximum divergence of the raster scanned beam is  $20^\circ$  and the sweep rate has a range of 0Hz to 500Hz. We typically use smaller divergence rastering  $\sim 10^\circ$  in order to uniformly expose our samples, Fig. 12.

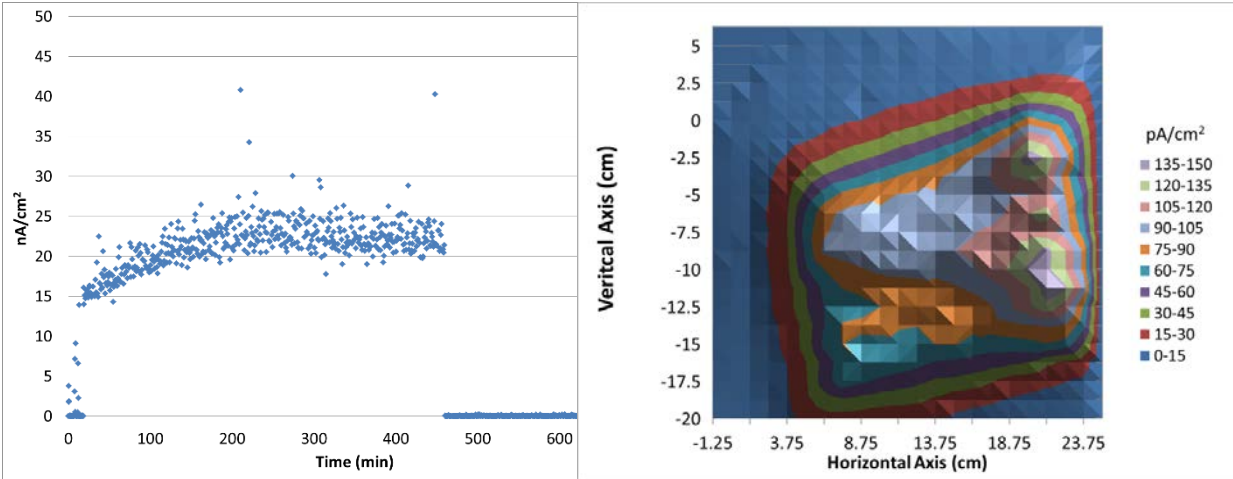


Figure 11 Electron beam flux at 90keV with rastering as a function of time. Figure 12 Beam Map of 20keV electrons with rastering.

The electron gun is also capable of running in pulsed mode. Although this capability is not currently in use, it provides the opportunity to look at materials exposed to highly controlled short bursts of electrons. This capability can be used to produce a continuous beam, single pulses of 2 $\mu$ s or a pulse train with a maximum frequency of 5kHz.

To measure the electron beam spot uniformity, maps are made using a Faraday cup mounted on the 2 axis translation stage. The position of the faraday cup is controlled with the stepper motors recording an average Faraday cup reading at each point. There is an extensive automated program capable of moving the translational stages in discrete steps and recording the readings of various probes in Jumbo. This allows us to record the flux of various particles as a function of spatial location. This is critical to obtaining a precise knowledge of the environment to which we are exposing our samples to in Jumbo. The long term stability of the electron gun has also been determined by leaving the Faraday cup at a single point and recording the current as a function of time. This indicates that the rastering occurs on a time scale shorter than 0.5 seconds, much faster than the rotation of our wheel and consequently does not cause inaccuracy in our fluence calculations.

The beam shape is steady over long periods of time including multiple vent cycles of the electron gun. Additionally, during material exposure to the electron beam the flux is recorded using the Faraday cup. This gives a very accurate measurement of the absolute flux which is critical for calculating the amount of aging and is also used in the fitting of charge/discharge curves of materials under investigation.

In addition to using the electron gun to test the charge transport characteristics of materials it is also used to age materials. A high energy on the electron gun, 90keV, is used to fully penetrate the thin materials we are studying here. Monte-Carlo simulation of energy loss per unit length was performed with Monte Carlo N-Particle Code, v. 6.1 (MCNP6.1) [60] in order to accurately characterize the electron dose profile in PI. In this simulation, 20 million 90 keV electrons impinged on a 76  $\mu$ m thick Kapton film backed by an aluminum layer of infinite thickness. The simulation results presented in Figure 14 show the average energy deposition per electron per 1

$\mu\text{m}$  thick Kapton layer. Backscattering and bremsstrahlung were also accounted for in the simulation. According to the simulation, the average energy deposited in PI per electron per  $\mu\text{m}$  is 1.08 keV. The continuous slowdown approximation (CSDA) from the NIST EStar database [61] predicts an average energy deposition of 0.99 keV/  $\mu\text{m}$ .

The gun flux is capable of simulating 12 months of dose in an average GEO environment in 4 hours over our entire sample wheel, with a beam map shown in Fig. 13. This allows for the creation of highly aged materials in a short period of time.

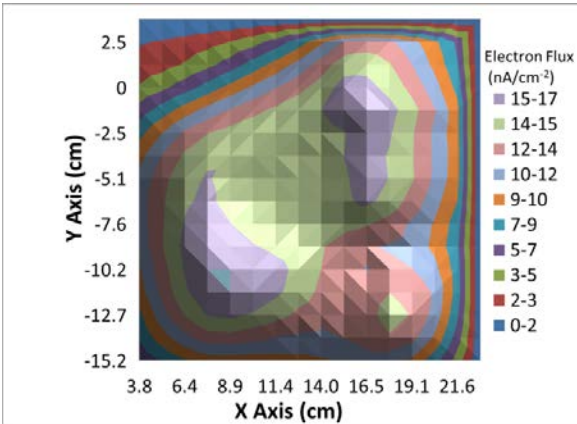


Figure 13 Beam map of 90 keV rastered electron beam.

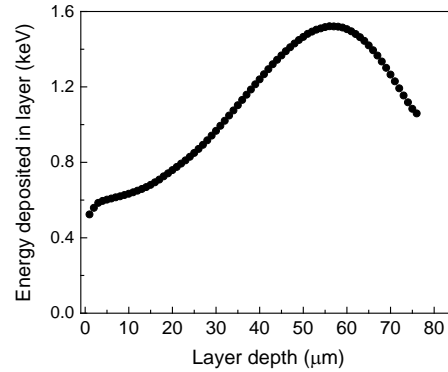


Figure 14 Energy deposited in 76  $\mu\text{m}$  Kapton by 90 keV electron beam.

All aspects of Jumbo are controlled with LabVIEW, Fig. 15. The program controls the rotation of the sample carousel, controls the various sources in our chamber, and monitors the outputs from the various probes. This automation gives the capability to record the surface potential of various materials using the surface potential probe while rotating the sample holder and controlling the flux of electrons on the materials to determine the extent to which they charge. The control software is robust and allows for continuous testing for weeks without human supervision.

The rotating sample wheel exposes all samples on the wheel to the same environment. To test this, we placed three samples of 2 mil polyimide (PI) backed with Al on the sample wheel at different positions and exposed them to 20 keV electrons and measured their surface potential as a function time. A deep understanding of the physics in play is not necessary to see that all of the samples behave in the same manner, Fig. 16. This shows that sample location does not play a role in the environment that the samples are exposed to.



Figure 15 Front panel of LabVIEW automated control program.

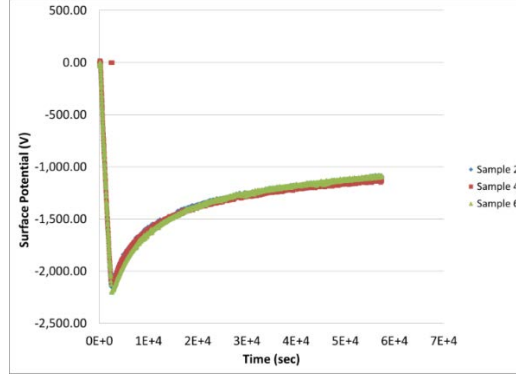


Figure 16 Charge and discharge curves for three identical samples of PI mounted at different positions on the sample wheel

### 3.3. MINION Long Duration Testing Chamber

The MINION chamber is a 0.91 m diameter by 1.14 m tall vacuum chamber with a total internal working volume of  $\sim 0.75 \text{ m}^3$  shown in Fig 17. This is a fully dry pumped system with a Varian TV1001 Navigator turbomolecular pump backed by a Varian Triscroll 600 rough pump.

This chamber can reach a base pressure of  $1 \times 10^{-6}$  torr in 30 minutes after vacuum break and mid  $10^{-7}$  torr overnight. Samples are mounted on a fixed plate in the chamber and probes are moved into place using a single Phytron stepper motor. This motor can move a Trek 370 surface potential probe ( $\pm 3 \text{ kV}$  range) and a Faraday cup mounted at opposite ends of a propeller-shaped bracket.



Figure 17 The exterior and interior of MINION chamber

This chamber is not intended to simulate space radiation, but rather simply charge materials and measure the surface potential decay rate. As such it has a 5 keV Kimball EGPS 2017B focusable electron gun used for charging materials and one VUV photon source of the same type as described above for discharging. All data acquisition and vacuum systems are controlled by LabVIEW and have a high degree of automation to facilitate month-long data runs.

## **4. EXPERIMENTAL RESULTS AND ANALYSIS**

As mentioned in section two, we have investigated the phenomenon of aging from the perspective of both charge transport (electrical conductivity) and optical response (absorption, transmission and reflection). The results of these investigations will be presented here as well as our interpretation of the chemical structure modifications caused by electron radiation damage.

Although this work has focused primarily on polyimide, low density polyethylene (LDPE) and Polyethylene terephthalate (PET, Mylar) were also investigated. Because of the complexity of each data set acquired, we have chosen to pursue in-depth studies of PI rather than cursory treatment of all three materials. That being said, some data for LDPE and PET will be presented here, however there is not enough data for deep interpretation.

All materials were aged in the Jumbo vacuum chamber and then moved to other facilities for characterization. We employed several techniques for understanding the charge transport and the chemistry of radiation damaged materials. These include conductivity measurements, UV/VIS absorption, FTIR, and EPR.

### **4.1. Polyimide**

Transmittance spectra of Kapton-H® films in UV/VIS spectral range measured right after electron bombardment with different doses are presented in Fig 18. For all radiation-damaged films transmittance was significantly lower compared to pristine material, which correlates with the darkening of damaged PI demonstrated in all studied samples and illustrated in the inset to Fig 18. Another important change identified on the UV/Vis spectra of irradiated material is the shift of fundamental bandgap, as shown in Fig 19. The observed reduction of the PI bandgap may be attributed to the population of additional radiation-induced defect states within the bandgap of irradiated material.

The transmittance spectra of electron-irradiated PI with dose of  $5.6 \times 10^7$  Gy (25 years in GEO equivalent) measured after 260 min of air exposure in UV/visible spectral range are presented in Fig 20. The transmittance spectrum of reference pristine PI material is also presented. A decrease in the optical bandgap observed for the radiation damaged material tends to return to nearly that of the pristine material with increased air exposure. It should be noted that transmittance of PIs irradiated with lower doses returns to the level of pristine material after prolonged air exposure (hours); PI damaged with higher dose does not fully recover even after very long air exposure.

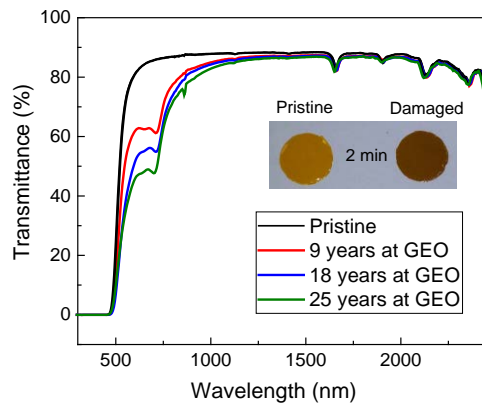


Figure 18 Transmittance spectra of reference (pristine) PI film and radiation damaged PI at different doses. Inset shows photographs of a pristine PI (left) and a radiation damaged with dose of  $5.6 \times 10^7$  Gy PI sample (right) after 2 minutes of air exposure. Changes of the material's optical behavior in the visible spectrum are obvious.

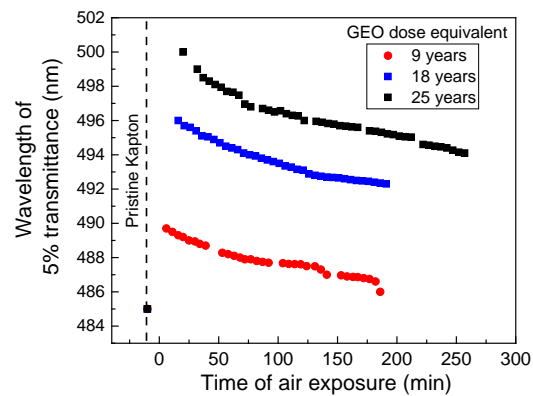


Figure 19 Change of fundamental bandgap of radiation-damaged PI at different GEO dose equivalents.

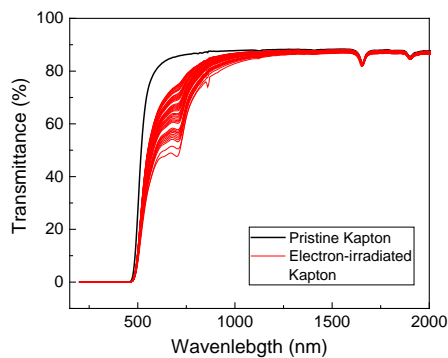


Figure 20 Transmittance spectra of radiation-damaged PI with  $5.6 \times 10^7$  Gy dose measured after (20-260) min of air exposure.

To quantify changes in the chemical structure of the electron-irradiated PI, IR absorption spectra were taken immediately after the samples were damaged with electrons. PI has a complex IR signature with each peak corresponding to a specific vibration within the monomer. Spectral directional hemispherical reflectance (DHR) was measured for pristine and electron radiation-damaged PI material with  $5.6 \times 10^7$  Gy, then absorbance was calculated assuming no light is transmitted. Figure 21 shows the IR absorbance spectra of reference (pristine) and electron-damaged PI with  $5.6 \times 10^7$  Gy. Air exposure prior to measurements was limited to 12 min, but

could not be completely eliminated so it must be assumed that some degree of recovery has taken place.

To help identify specific absorption bands of damaged PI material the second derivative of the corresponding absorbance spectrum was taken, as illustrated in Fig 22. Derivative spectroscopy allows easier peak identification due to the suppression of broad bands relative to the sharp bands. In addition, derivative spectroscopy eliminates baseline shift effects in measured spectra, thus improving the accuracy of quantification. Several common absorption peaks were identified; phenyl ring deformation  $\sigma(\text{phenyl ring})$  at  $945\text{ cm}^{-1}$ , bridging ether stretch  $\nu(\text{C-O-C})$  at  $1261\text{ cm}^{-1}$ , phenyl ring C-C stretch  $\nu(\text{phenyl ring})$  at  $1495\text{ cm}^{-1}$  and  $1601\text{ cm}^{-1}$ , imide stretch  $\sigma(\text{C-N-C})$  at  $365\text{ cm}^{-1}$ , and out-of-phase carbonyl stretch  $\nu(\text{C=O})$  at  $1896\text{ cm}^{-1}$ .

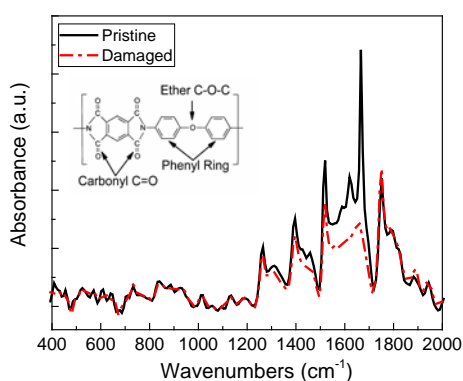


Figure 21 Absorbance spectra of pristine and electron radiation-damaged PI after 20 min of air exposure. Inset shows the schematic of PI's monomer with chemical constituents highlighted for reference.

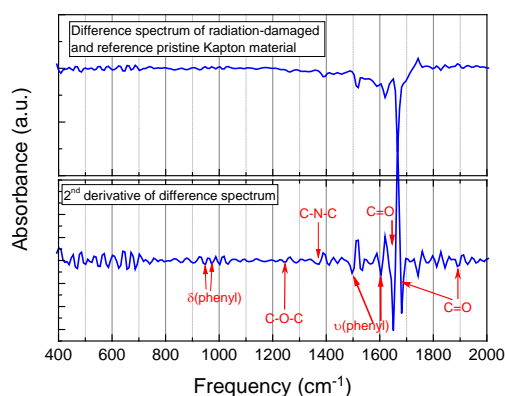


Figure 22 Top – difference spectrum of radiation-damaged and pristine PI material. Bottom – the 2<sup>nd</sup> derivative of difference spectrum. Several absorption bands are identified.

The intensity of selected tabulated absorption peak values plotted as a function of time exposure to air is shown in Fig 23 for electron radiation-damaged PI material with  $5.6 \times 10^7$  Gy dose. The same analysis with similar results was performed for PIs irradiated with lower doses.

This analysis indicates that not all pieces of the PI monomer are equally susceptible to electron induced damage. After electron-radiation induced damage of PI, an increase in carbonyl (C=O) absorption is observed, suggesting that none of the original carbonyls are being lost from the structure. New carbonyl bonds can only be formed by breaking of one C-O bond of ether (C-O-C). Accordingly, the absorption at the ether stretching frequency is reduced immediately after damage and recovers to near pristine levels at the same time scale as the carbonyl stretch. Next, the absorption at the phenyl ring stretching frequency,  $\nu(\text{phenyl})$ , after damaging is significantly lower than that in the pristine material on the same time scale. This is caused by electron induced bond rupture which has a high probability of forming one or more radicals which have an electron to donate to the new carbonyl bond. As the other components of the molecule return to their pristine state, the phenyl absorption also recovers, indicating healing of the phenyl rings. The absorption at the phenyl ring deformation frequency,  $\sigma(\text{phenyl})$ , is increased compared to the pristine material.

Finally, we found that electron irradiation enhances the absorption at the imide stretching  $\sigma(\text{C-N-C})$  frequency. Radiation-induced bond breakage between nitrogen (N) and carbon (C) could change the dipole moment of the remaining C-N bond of imide, and this will manifest itself in increased absorption.

Surface potential decay measurements were performed on radiation-damaged PI in vacuum. To monitor vacuum recovery (healing) of the radiation-damaged PI, measurements were performed over several weeks with  $\sim 2$  day time intervals. Fig 24 demonstrates the sample normalized potential versus time curve for the surface potential decay of electron-irradiated PI.

The initial values of free parameters  $r_r$ ,  $r_t$ ,  $a$ ,  $\alpha$ ,  $\beta$ , and  $\mu_0$  from Eq. 4 were estimated from the bibliography to provide the starting point for the fit.[62] Selected values of free parameters, carrier mobility in the damaged PI, as well as probabilities of charge being released and re-trapped in different trapping center, are plotted in Fig 25 as a function of vacuum exposure, and compared with the corresponding values of pristine Kapton. No significant variation of carrier mobility was observed after five weeks of vacuum exposure, suggesting that the radiation-damaged material retains its properties in vacuum. Compared to pristine Kapton, carrier mobility and probability of charge being re-trapped by different charge trap did not change, whereas probability of charge being released from a trap is significantly increased.

To evaluate the radical concentration of radiation-damaged material, immediately after irradiation, damaged Kapton with a dose of  $4.0 \times 10^7$  Gy (18 year GEO equivalent) was sealed in a vacuum tube and shipped to Hunter College of the City University of New York for the EPR measurements. Due to the interaction of nitrogen and oxygen in aromatic rings of Kapton with high energy electrons, radicals are formed upon irradiation. Radical concentration in irradiated Kapton was measured as  $\sim 3 \times 10^{17}$  spins/gram, as shown in Figure 26. An undamaged reference sample showed no EPR signal indicating that there are no unpaired electrons present in pristine PI, as was expected. However, a strong initial EPR signal was measured in the damaged material, with the

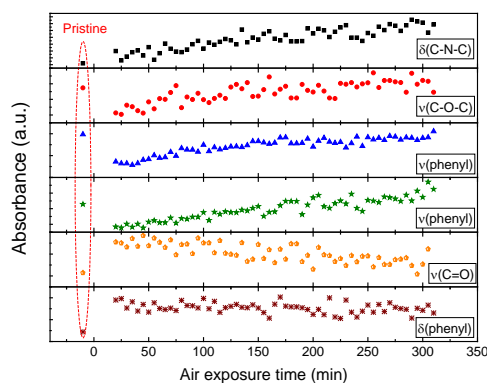


Figure 23 Intensity of selected absorption bands of radiation damaged PI with  $5.6 \times 10^7$  Gy dose as a function of air exposure time.

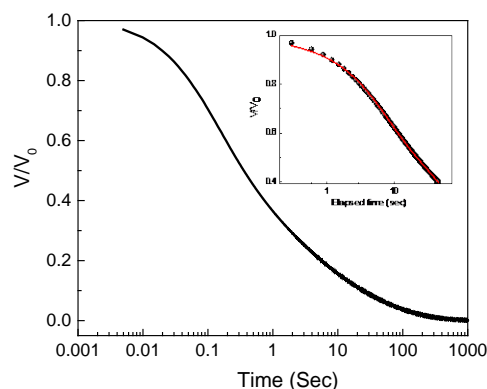


Figure 24 Normalized surface potential versus time. Inset illustrates fitting of pre-transit region of potential decay curve to Eq. (4).

EPR signal not degrading significantly in vacuum. Oppositely, we showed earlier that the intensity

of the EPR signal decays with increased air-expose of the damaged material.[64]

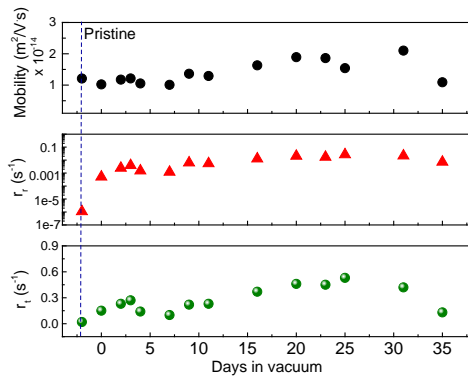


Figure 25 Selected parameters ( $\mu_0$  (mobility),  $r_r$  (release probability), and  $r_t$  (trapping probability)) obtained from fitting of Eq. (4) to the surface potential discharge curves as a function of vacuum exposure.

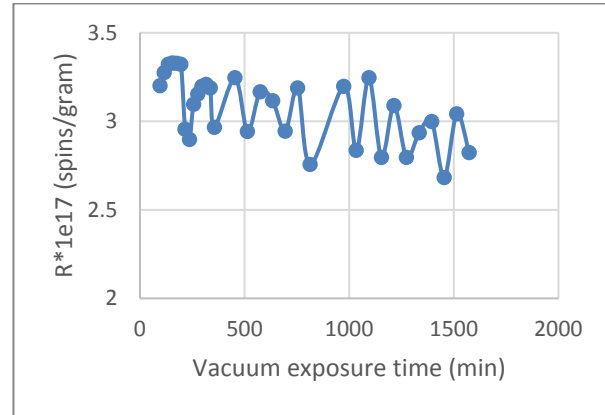


Figure 26 Radical concentration of radiation-damaged Kapton with a dose of  $4.0 \times 10^7$  Gy as a function of vacuum exposure.

Finally, resistivity of radiation-damaged material was evaluated using volume resistivity measurements and surface potential decay curves, as shown in Figures 27 and 28. Considering a post-transit region of surface potential decay curves, defined as when a charge body reaches the back plane, a decay time and the dark resistivity of the material was derived using Eq. 5. Air exposure of radiation-damaged PI resulted in fast recovery, i.e. within 3 hours of irradiation the PI's resistivity changed from  $1.2 \times 10^{14} \Omega\cdot m$  to that of pristine PI ( $4.7 \times 10^{17} \Omega\cdot m$ ), whereas the

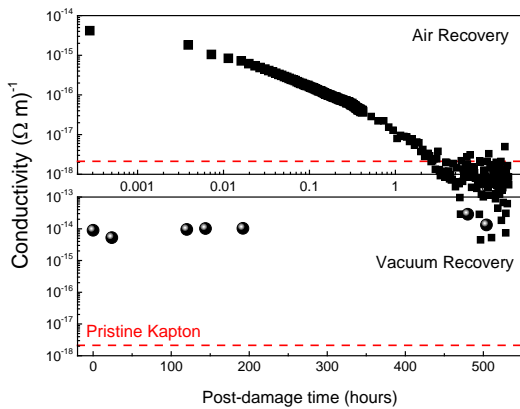


Figure 27 Comparison of air- and vacuum-recovered conductivities of Kapton irradiated with electron dose of  $5.6 \times 10^7$  Gy. Dashed line presents conductivity of undamaged (pristine) PI.

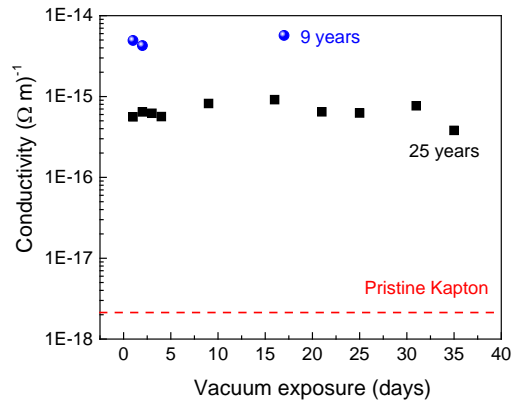
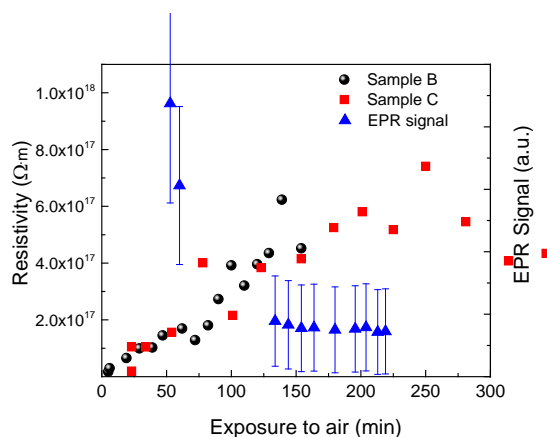


Figure 28 Conductivity of radiation-damaged Kapton with electron dose of  $5.6 \times 10^7$  Gy as a function of vacuum exposure.

vacuum recovery of radiation-damaged PI retained the same value,  $\sim 1 \times 10^{14} \Omega\cdot\text{m}$ , even three weeks (504 hours) after damage.

To further probe the effects of air exposure on resistivity of radiation-damaged PI, the volume conductivity of three radiation damaged (with dose of  $5.6 \times 10^7 \text{ Gy}$ ) PI samples was measured: sample A was stored in air after electron damage; sample B was stored under vacuum and only exposed to air during conductivity measurements; sample C was stored in a separate vacuum chamber between measurements that could be vented and pumped down more quickly than that in which sample B was stored. Sample A demonstrated recovery to a stable resistivity of  $1 \times 10^{18} \Omega\cdot\text{m}$  within the first  $\sim 150 \text{ min}$  of air exposure. Samples B and C recovered to the resistivity of  $6 \times 10^{17} \Omega\cdot\text{m}$  after 250 hrs and 400 hrs in vacuum, respectively. The resistivity of samples B and C as a function of cumulative air exposure time is plotted in Fig 29.



*Figure 29 Resistivity (inverse of conductivity) and EPR signal of radiation damaged PI film plotted as a function of cumulative air exposure time. EPR normalized to steady state radical concentration.*

Further, during the same time period that the resistivity was being measured EPR measurements were performed on the damaged material and a pristine reference sample to determine the concentration of unpaired electrons in the damaged material. EPR data for the radiation damaged PI are also plotted in Figure 29.

EPR shows that the decay of the radical signal occurred on the same air-exposure time scale as the increase in resistivity after initial electron induced damage. This suggests that these radicals are involved in the transport of electrons through the bulk of the material. Clearly they are reactive; as they react, the resistivity trends back toward its initial value.

More information about the chemistry occurring in PI during electron irradiation was obtained using X-Ray Photoelectron Spectrometry (XPS) measurements. XPS is only sensitive to the first few layers of the material, however due to the nature of the electron energy loss mechanism, it is likely that the surface chemistry closely mimics that of the bulk. XPS yields elemental composition of the sample as well as bonding information on the individual components. It should be noted that all XPS data presented here are assumed to be fully healed in the presence of atmosphere. The two most striking XPS results are shown in Figure 30. The XPS shows a decrease in the elemental

fraction of oxygen in a sample with a  $5 \times 10^5$  Gy electron exposure versus that of the pristine material, which then increases with further aging. The measured oxygen is below the fraction dictated by the stoichiometry of the monomer unit. This could be due to molecular orientation on the surface. It is possible, although unlikely, that this is due to material contamination. Similar elemental composition measurements on pristine samples using XPS has been previously seen with oxygen representing 15.1% of the composition.[64] The fraction of carbon that is bound to a nitrogen or oxygen atom also undergoes an initial drop followed by a recovery to near the pristine state. We noted a dramatic increase in chamber pressure during aging and we attribute it to outgassing of species that have been created by bonds breaking in the PI. As time progresses the chamber pressure drops, indicating decreased outgassing, however it does not return to its baseline. This indicates that gas evolution from PI plays an important role in the chemistry of PI. To understand the change in elemental composition we draw on two different studies of irradiation PI and evolution of gaseous species from these samples. These studies were undertaken with very different conditions, both from each other, and from our set-up, but the chemistry they propose is consistent with the measurements here.

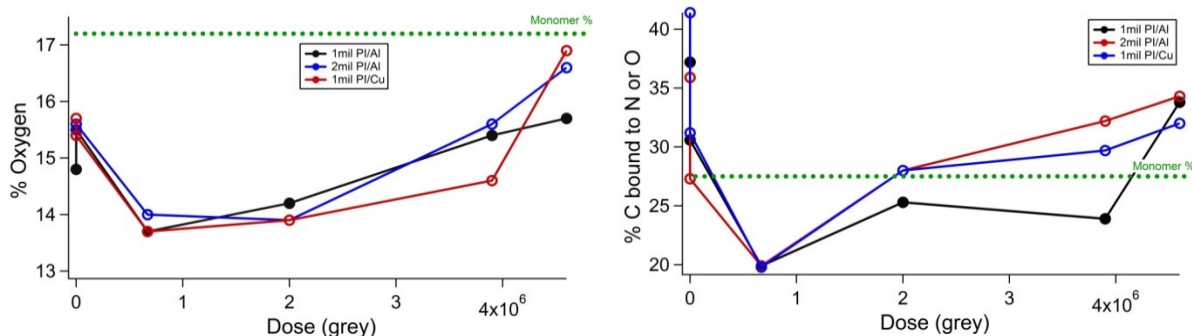


*Figure 30 XPS results on PI as a function of dose. (left) The elemental fraction of oxygen in the PI for three different samples 1mil PI backed by Al, black, 2 mil PI backed by Al, red, and 1mil PI backed with Cu tape, blue. The theoretical fraction is shown as a dashed green line. (right) The fraction of carbon that is electron poor for the same three PI samples.*

These studies were undertaken with different energetic particles and cover a wide range of energies, but the chemistry they propose is consistent with the measurements here. Oxygen is lost as  $\text{CO}$ ,  $\text{CO}_2$ , and  $\text{H}_2$ , is evolved from the material.[21] Our XPS results indicate the oxygen that has double or triple bonds is preferentially lost versus only single-bonded oxygen, which is in line with our theory and the results seen in the IR absorption of  $50 \mu\text{m}$  material. Decreases in oxygen to 12% have been previously seen in proton bombardment, and although we don't see this extent of change our results agree qualitatively. [65] Other PI degradation experiments found that with 760 MeV Kr ion bombardment the major gas species evolved from the system were mainly hydro-deficient chain fragments of the form of  $\text{C}_x\text{H}_{2x-y}$  ( $x$  varies from 1 to 6, for each  $x$ , there are several  $y$ ). It is likely that both of these mechanisms play a role in the degradation chemistry, but that the relative importance of each varies with dose.

It is important to reiterate that the XPS data shown here was taken after the materials have been exposed to >>150 min of air. It is assumed that these materials are fully recovered after their extended exposure to atmosphere.

## 4.2. LDPE and Mylar

Three materials were studied and while the bulk of the analysis was done on PI there still exist some intriguing results on low density polyethylene (LDPE) and Mylar (Polyethylene terephthalate, PET) that remain to be explored. A qualitative summary will be give below with a full quantitative analysis to be published in the future.

LDPE was included in this study not because of its relevance to spacecraft construction but rather because of its relatively simple chemistry, semi-crystalline structure and ubiquity in the literature.[42, 63] Charge/discharge curves were taken of pristine LDPE and showed a complex charge-up curve that we postulate arises from the low charging beam current causing the charge time to be roughly on the order of the transit time. This is due to the fact that during charge up the steady state voltage is the time when the electron beam induced charging is in balance with the charge leaking through the material. Under these circumstances, the incident current is constant (electron beam), but as the front of the charge body reaches the backplane the discharge current changes. This manifests itself as a time-variant steady-state surface potential. In future studies, the charging beam flux will be increased to  $\sim 10^{-8}$  A/cm<sup>2</sup> to charge the material on a time scale much faster than the transit time of a few hours. In the experiments described here, pristine LDPE reached a relatively steady surface potential at -300 V during charge up using a 20 keV electron beam with a flux of 50 pA/cm<sup>2</sup>.

The charging data for LDPE is difficult to interpret for the reasons stated above. However, the discharge data is relatively straightforward, yielding a resistivity of  $9 \times 10^{19}$   $\Omega$ -m and in good agreement of the manufacture value of  $5 \times 10^{19}$   $\Omega$ -m. When aged with a 90 keV electron beam and total dose of  $7 \times 10^5$  Gy (equivalent to 1.2 months in GEO) the resistivity dropped to  $6 \times 10^{17}$   $\Omega$ -m. This trend continued with a further decrease in resistivity to  $3 \times 10^{17}$   $\Omega$ -m after  $3.9 \times 10^6$  Gy (6.8 months in GEO). These two aging runs were also accompanied by an increase in the steady state voltage achieved during charging of -1 kV and -3kV respectively. We theorize that, as with PI, electron damage creates new electron trap states that aid in the conduction of trapped electrons by virtue of an increased electronic DOS in the material's bandgap. Concomitantly, these trap states provide more places for electrons to reside during charge up leading to a higher steady state surface voltage. After further irradiation with  $4.7 \times 10^6$  Gy (8.3 months in GEO), the trend in the steady state surface potential continued with and increase to -5 kV during charge up, however the discharge curve showed that the resistivity increased to  $6 \times 10^{18}$   $\Omega$ -m from the  $3.9 \times 10^6$  Gy dose. We postulate that during the early phases of aging the material becomes less resistive because an increased DOS facilitates electron capture and transport; however, after some damage threshold, the semi-crystalline domains present in pristine LDPE begin to break down. The destruction of the long-range order results in an increased resistivity in the material.

Space-rated 25 $\mu$ m Al-backed PET provided to us by Sheldahl was also tested. This material was charged with a 20 keV electron beam with a flux of 50 pA/cm<sup>2</sup>, but wasn't allowed to reach steady state because the voltage was well above -5 kV leading to an increased risk of electrostatic breakdown. For this reason, little information was derived from the charge up curve. However, the

discharge curve yielded some interesting results. We calculated the bulk resistivity to be  $4 \times 10^{20}$   $\Omega$ -m, the highest resistivity measured in any material this study. Interestingly, PET shows the opposite behavior of PI as it ages by becoming more resistive. When aged with a 90 keV electron beam and total dose of  $7 \times 10^5$  Gy (equivalent to 1.2 months in GEO) the resistivity increased to  $1 \times 10^{21}$   $\Omega$ -m. This trend continued as the material was exposed to  $3.9 \times 10^6$  Gy and  $4.7 \times 10^6$  Gy with increases in resistivity to  $3 \times 10^{21}$   $\Omega$ -m and  $7 \times 10^{22}$   $\Omega$ -m respectively. These calculated values should be viewed with some degree of caution because measuring decay rates over the months it would take for these materials to discharge is impractical. The general trend of the material becoming more resistive with increased electron induced damage is an intriguing result.

## 5. CONCLUSIONS

We investigated optical and transport properties of Kapton material irradiated with different electron doses of simulated GEO environment with optical absorption spectroscopy, EPR measurements, surface potential decay and volume conductivity measurements. Analysis of free parameters obtained from a mathematical fit of surface potential decay curves of electron-bombarded Kapton by Eq. (1) showed that carrier mobility and the charge trapping probability did not significantly differ from those of pristine material. However, the probability of charge to release from trap states was significantly higher for irradiated material. According to Toomer and Lewis, the release rate  $r_r$  is inversely related to the depth of traps

$$r_r = v \cdot \exp\left(-\frac{E_t}{kT}\right) \quad (6)$$

where  $v$  is the so-called attempt-to-escape frequency.

Thus, the significantly increased release rate in damaged material is suggesting the creation of a number of shallow electron traps as a result of high-energy electron bombardment. These shallow states may be attributed to the presence of unpaired electrons in damaged material, as revealed by EPR measurements. Possible origins of these free radicals formations may be deduced from IR absorption data.

After electron bombardment, an increase in carbonyl (C=O) absorption is observed, suggesting that none of the original carbonyls are being lost from the structure. New carbonyl bonds may only be formed by breaking one bond of the ether (C-O-C) group. Accordingly, the absorption at the ether stretching frequency is reduced immediately after damage and recovers to near pristine levels on the same time scale as the carbonyl stretch. Finally, absorption at the phenyl ring stretching frequency after damage shows an initial drop followed by a return to pristine levels on the same time scale. This suggests that damage causes scission of the phenyl rings and simultaneous formation of a new carbonyl functional group containing the ether oxygen. Scission of the phenyl rings is also the most promising candidate for radical formation. Thus, excessive radicals are likely originated from a radiation-induced breakage of phenyl rings and/or ether bridges forming a metastable carbonyl.

This study suggests that the presence of radicals plays a critical role in the transport of electrons through the bulk of the damaged material. Increased concentration of free radicals in conjunction

with increased probability of charge to be released from the trap in radiation-damaged material will lead to faster movement of charge body during surface potential decay measurements thus improving conductivity of the material. Additionally, UV-VIS transmission spectroscopy shows that the new damage induced electronic states within the bandgap decay on the same time scale as the apparent loss of radicals, suggesting that they are intimately related. Further, FTIR spectroscopy shows that phenyl ring scission and carbonyl formation are also occurring on the same timescale as the loss of the new electronic transitions and radical loss. It is from these common timescales that we draw the conclusion that electron damage causes phenyl ring scission preferentially followed by the formation of carbonyl with a delocalized radical associated with it. These radicals increases the density of energetically shallow trap states within the bandgap and intern enhance the electron mobility through the bulk.

## SUMMARY OF PUBLICATIONS AND PRESENTATIONS

*Table 1 Publications*

Title	Type	Venue	Date	Status
Jumbo Space Environment Simulation and Spacecraft Charging Chamber Characterization	AFRL Technical Report	Defense Technical Information Center	Feb 2015	Published
Minimally Invasive Modification of Conductivity in Insulators by Application of Radiation	Patent Disclosure	Internal document	March 2015	Awaiting review from KAFB patent lawyer. Expect progress ~2017
Changes of the Electrical and Optical Character of Polyimide Films (and the Chemistry that Drives Them) Due to Exposure to High Energy GEO-like Electrons	Conference Proceeding	Advanced Maui Optical and Space Surveillance Technology Conference	Sept 2015	Published
Effects of Radiation Damage on Polyimide Resistivity	Peer reviewed journal article	AIAA Journal of Spacecraft and Rockets	Dec 2015	Published
Chemical and Electrical Dynamics of Radiation Damaged Polyimide Film	Conference Proceeding	14th Spacecraft Charging Technology Conference	April 2016	Published

**Table 1 Publications (cont)**

Title	Type	Venue	Date	Status
Study of Kapton decomposition caused by electron beam irradiation	PhD Thesis Chapter	Department of Mechanical and Nuclear Engineering, Penn State	June 2016	PhD awarded
CHEMICAL AND ELECTRICAL DYNAMICS OF POLYIMIDE FILM DAMAGED BY ELECTRON RADIATION	Peer reviewed journal article	Special issue of IEEE transactions on plasma science	Sept 2016	Accepted for publication
Optical and Chemical Characterization of Polyimide in a GEO-like Environment	Conference Proceeding	Advanced Maui Optical and Space Surveillance Technology Conference	Sept 2016	Published
DEGRADATION OF POLYIMIDE UNDER ELECTRON IRRADIATION	Conference Proceeding	29th Space Simulation Conference	Nov 2016	Published
Degradation of polyimide under exposure to 90 keV electron	Peer reviewed journal article	Physica Status Solidi	Dec 2016	Accepted
EPR and NMR Studies on Damage and Recovery Mechanism of Electron-Irradiated Polyimide	Thesis Proposal	Department of Physics and Astronomy, Hunter College, CUNY	Jan 2017	Submitted for defense <b>(DRAFT)</b>
Effect of Atmosphere on Recovery Dynamics of Polyimide Film Damaged by Electron Radiation	Peer reviewed journal article	Undecided	Feb 2017	In preparation <b>(DRAFT)</b>
Optical Characterization of Common Spacecraft Materials after GEO-like Electron Bombardment	Abstract for conference proceeding	National Space and Missile Materials Symposium	June 2017	Abstract accepted

**Table 2 Presentations**

Venue	Date
1 <sup>st</sup> Quarter Materials Working Group (AFRL/RD)	Jan 2015
AFOSR Lab Days 2015	Jan 2015
Program Review <i>Aerospace Materials for Extreme Environments</i>	May 2015
Innovation Discovery Event	June 2015
Advanced Maui Optical and Space Surveillance Technology Conference	September 2015
Technology Quality Review	September 2015
Program Review <i>Aerospace Materials for Extreme Environments</i>	May 2016
14 <sup>th</sup> Spacecraft Charging Technology Conference	June 2016
29 <sup>th</sup> Space Simulation Conference	Nov 2016
Program Review <i>Remote Sensing and Imaging Physics</i>	Dec 2016
Science Advisory Board (SAB 2016)	Dec 2016

## References

1. Awaja, F., et al., *Surface molecular degradation of selected high performance polymer composites under low earth orbit environmental conditions*, Polymer degradation and stability, 2011, **96**(7), pp. 1301-1309.
2. Wei, Z., et al., *Erosion of a polyimide material exposed to simulated atomic oxygen environment*, Chinese Journal of Aeronautics, 2010, **23**(2), pp. 268-273.
3. Verker, R., et al., *Tensile stress effect on the macromolecular orientation and erosion mechanism of an atomic oxygen irradiated polyimide*, Polymer degradation and stability, 2013, **98**(5), pp. 997-1005.
4. Lei, X., et al., *Evolution of surface chemistry and morphology of hyperbranched polysiloxane polyimides in simulated atomic oxygen environment*, Corrosion Science, 2015, **98**, pp. 560-572.
5. Banks, B.A., et al., *Prediction of atomic oxygen erosion yield for spacecraft polymers*, Journal of Spacecraft and Rockets, 2011, **48**(1), pp. 14-22.
6. Shimamura, H., *Effects of LEO environment on mechanical properties of polyimide films under tensile strain*. in *Proceedings of International Symposium on "SM/MPAC & SEED Experiment,"* 2008, Tsukuba, Japan.
7. Shimamura, H. and T. Nakamura, *Investigation of degradation mechanisms in mechanical properties of polyimide films exposed to a low earth orbit environment*, Polymer Degradation and Stability, 2010, **95**(1), pp. 21-33.
8. Han, J.-H. and C.-G. Kim, *Low earth orbit space environment simulation and its effects on graphite/epoxy composites*, Composite structures, 2006, **72**(2), pp. 218-226.
9. Brunsvold, A.L., et al., *Beam-surface scattering studies of the individual and combined effects of VUV radiation and hyperthermal O, O<sub>2</sub>, or Ar on FEP teflon surfaces*, ACS applied materials & interfaces, 2008, **1**(1), pp. 187-196.
10. Minton, T.K., et al., *Atomic oxygen effects on POSS polyimides in low earth orbit*, ACS applied materials & interfaces, 2012, **4**(2), pp. 492-502.
11. Xiao, F., K. Wang, and M. Zhan, *Atomic oxygen erosion resistance of polyimide/ZrO<sub>2</sub> hybrid films*, Applied Surface Science, 2010, **256**(24), pp. 7384-7388.
12. Son, G.C.-G.K., *Protective effect of nanocomposite film from the low earth orbit environment*, Journal of Composite Materials, 2016, **49**(19), pp. 2297-2306.
13. Gouzman, I., et al., *Thin film oxide barrier layers: protection of Kapton from space environment by liquid phase deposition of titanium oxide*, ACS Applied Materials & Interfaces, 2010, **2**(7), pp. 1835-1843.
14. Xiao, F., K. Wang, and M.S. Zhan, *Atomic oxygen resistant phosphorus-containing polyimides for LEO environment*, Journal of Materials Science, 2012, **47**(12), pp. 4904-4913.
15. Fischer, H.R., et al., *Development of flexible LEO-resistant pi films for space applications using a self-healing mechanism by surface-directed phase separation of block copolymers*, ACS applied materials & interfaces, 2010, **2**(8), pp. 2218-2225.
16. Fukunaga, K. and T. Maeno, *Space charge observation of polyimide films under DC electric fields*, in *Solid Dielectrics, 2004, ICSD 2004, Proceedings of the 2004 IEEE International Conference on*, 5-9 July 2004, Tordouce, France.

17. Zhou, L., et al., *Study on charge transport mechanism and space charge characteristics of polyimide films*, Dielectrics and Electrical Insulation, IEEE Transactions on, 2009, **16**(4), pp. 1143-1149.
18. Levy, L., et al., *Aging and Prompt Effects on Space Material Properties*, Plasma Science, IEEE Transactions on, 2008, **36**(5), pp. 2228-2237.
19. Hanna, R., et al., *Radiation induced conductivity in space dielectric materials*, Journal of Applied Physics, 2014, **115**(3), p. 033713.
20. Sharma, A. and N. Sridhara, *Degradation of thermal control materials under a simulated radiative space environment*, Advances in Space Research, 2012, **50**(10), pp. 1411-1424.
21. Ennis, C.P. and R.I. Kaiser, *Mechanistical studies on the electron-induced degradation of polymethylmethacrylate and Kapton*, Physical Chemistry Chemical Physics, 2010, **12**(45), pp. 14902-14915.
22. Lai, S.T., *Importance of surface conditions for spacecraft charging*, Journal of Spacecraft and Rockets, 2010, **47**(4), pp. 634-638.
23. Arkhipov, V., J.A. Popova, and A. Rudenko, *Space-charge perturbed dispersive transport in disordered dielectrics*, Journal of Electrostatics, 1986, **18**(1), pp. 23-37.
24. Yadlowsky, E.J. and R.C. Hazelton, *Radiation induced conduction in Kapton H film*, IEEE Transactions on Nuclear Science, 1988, **35**(4), pp. 1050-1054.
25. Frederickson, A., S. Woolf, and J. Garth, *Model for space charge evolution and dose in irradiated insulators at high electric fields*, IEEE Transactions on Nuclear Science, 1993, **40**(6), pp. 1393-1401.
26. Perrin, C., et al., *Analysis of internal charge distribution in electron irradiated polyethylene and polyimide films using a new experimental method*, Journal of Physics D: Applied Physics, 2008, **41**(20), p. 205417.
27. Paulmier, T., et al., *Material Charging in Space Environment: Experimental Test Simulation and Induced Conductive Mechanisms*. Dielectrics and Electrical Insulation, IEEE Transactions on, 2009, **16**(3), pp. 682-688.
28. Nitta, K. and M. Takahashi, *Material Properties Measurements Related to Spacecraft Charging/Discharging*, IEEJ Transactions on Fundamentals and Materials, 2009, **129**, pp. 739-745.
29. Lai, S.T., *A critical overview on spacecraft charging mitigation methods*, IEEE Transactions on Plasma Science, 2003, **31**(6), pp. 1118-1124.
30. Watson, P.K., *The Transport and Trapping of Electrons in Polymers*, IEEE Transactions on Dielectrics and Electrical Insulation, 1995, **2**(5), pp. 915-924.
31. Sim, A., *Unified model of charge transport in insulating polymeric materials*, in *Physics*, 2013, Utah State University, Logan, UT.
32. Wintle, H., *Conduction processes in polymers*, in *Engineering Dielectrics Volume IIA Electrical Properties of Solid Insulating Materials: Molecular Structure and Electrical Behavior*, 1983, ASTM International, Philadelphia, PA.
33. Wintle, H., *The motion of electric charges on and near insulator surfaces*, Le Vide, 1998, **53**(287), pp. 49-58.
34. Leach, R.D., M.B.A., *Failures and Anomalies Attributed to Spacecraft Charging*, in *Reference Publication*, 1995, NASA.
35. Horowitz, G., *Organic field-effect transistors*, Advanced Materials, 1998, **10**(5), pp. 365-377.

36. Pepin, M.P. and H.J. Wintle, *Charge injection and conduction on the surface of insulators*, Journal of Applied Physics, 1998, **83**(11), pp. 5870-5879.
37. Wintle, H.J., *The motion of electric charges on and near insulator surfaces*, Vide Science, Technique et Applications, 1998, pp. 49-58.
38. Wintle, H.J., *Conduction Processes in Polymers*, in *Electrical Properties of Solid Insulating Materials: Molecular Structure and Electrical Behavior*, R. Bartnikas, Editor. 1983, American Society for Testing and Materials, Philadelphia, PA.
39. Hoffmann, R., et al., *Low-Fluence Electron Yields of Highly Insulating Materials*, IEEE Transactions on Plasma Science, 2008, **36**(5), pp. 2238-2245.
40. Blaise, G., *Charge localization and transport in disordered dielectric materials*, Journal of Electrostatics, 2001, **50**(2), pp. 69-89.
41. Dennison, J., et al., *Radiation Induced Conductivity of Highly-Insulating Spacecraft Materials*, in *10th Spacecraft Charging Technology Conference*, 2009, Biarritz, France.
42. Brunson, J., *Hopping conductivity and charge transport in low density polyethylene*, in *Physics*, 2010, Utah State University, Logan, UT.
43. Hoffmann, R.C., et al., *The Correlation Between Radiation Induced Conductivity (RIC) and Electron Beam Induced Luminescence in Disordered SiO<sub>2</sub>*, in *11th IEEE International Conference on Solid Dielectrics*, 2013, Bologna, Italy.
44. Frederickson, A.R., C.E. Benson, and J.F. Bockman, *Measurement of charge storage and leakage in polyimides*, Nuclear Instruments and Methods in Physics Research Section B: Beam Interactions with Materials and Atoms, 2003, **208**, pp. 454-460.
45. Frederickson, A.R. and J. Dennison, *Measurement of conductivity and charge storage in insulators related to spacecraft charging*, IEEE Transactions on Nuclear Science, 2003, **50**(6), pp. 2284-2291.
46. Dennison, J.R., et al., *Methods for high resistivity measurements related to spacecraft-charging*, IEEE transactions on plasma science, 2006, **34**(5), pp. 2191-2203.
47. Fowler, J.F. *X-ray induced conductivity in insulating materials*, in *Proceedings of the Royal Society of London A: Mathematical, Physical and Engineering Sciences*, 1956, The Royal Society, London, England.
48. Coelho, R., L. Levy, and D. Sarrail, *Charge decay measurements and injection in insulators*, Journal of Physics D: Applied Physics, 1989, **22**(9), p. 1406.
49. Cazaux, J., *Some considerations on the secondary electron emission,  $\delta$ , from  $e^-$  irradiated insulators*, Journal of Applied Physics, 1999, **85**(2), pp. 1137-1147.
50. Meyza, X., et al., *Secondary electron emission and self-consistent charge transport and storage in bulk insulators: Application to alumina*, Journal of Applied Physics, 2003, **94**(8), pp. 5384-5392.
51. Hodges, J., *In situ measurements of electron-beam-induced surface voltage of highly resistive materials*, in *Physics Department*, 2012, Utah State University, Logan, UT, p. 139.
52. Song, Z., C. Ong, and H. Gong, *Secondary and backscattered electron yields of polymer surface under electron beam irradiation*, Applied Surface Science, 1997, **119**(1), pp. 169-175.
53. Hoffmann, R., et al., *Low-fluence Electron Yields of Highly Insulating Materials*, Plasma Science, IEEE Transactions on, 2008, **36**(5), pp. 2238-2245.
54. Toomer, R. and T. Lewis, *Charge trapping in corona-charge polyethylene films*, Journal of Physics D: Applied Physics, 1980, **13**(7), pp. 1343.

55. Smith, R.A., *Semiconductors*, 2nd ed., 1979, Cambridge University Press, London, England.
56. Cohen, M. and J.R. Chelikowsky, *Electronic structure and optical properties of semiconductors*, Vol. 75, 2012, Springer Science & Business Media, Berlin, Germany.
57. Peter, Y. and M. Cardona, *Fundamentals of semiconductors: physics and materials properties*, 2010, Springer Science & Business Media, Berlin, Germany.
58. Lean, J. and A. Skumanich, *Variability of the Lyman alpha flux with solar activity*, *Journal of Geophysical Research: Space Physics* (1978-2012), 1983, **88**(A7), pp. 5751-5759.
59. Ginet, G.P., et al., *AE9, AP9 and SPM: New Models for Specifying the Trapped Energetic Particle and Space Plasma Environment*, *Space Science Reviews*, 2013, **179**(1-4), pp. 579-615.
60. Mosteller, R.D., *Bibliography of MCNP Verification & Validation: 1990-2003*, LA-UR-03-9032, Los Alamos National Laboratory, Los Alamos, NM, 2003.
61. Berger, M., *ESTAR, PSTAR, and ASTAR: Computer programs for calculating stopping-power and range tables for electrons, protons, and helium ions*, Unknown, 1992. **1**.
62. Aragonese, A., et al., *Effect of humidity in charge formation and transport LDPE*, *Journal of Electrostatics*, 2013, **71**(4), pp. 611-617.
63. Engelhart, D., et al., *Chemical and Electrical Dynamics of Polyimide Film Damaged by Electron Radiation*, in *14th Spacecraft Charging Technology Conference, ESA/ESTEC*, Noordwijk, NL, 2016.
64. Cooper, R., et al., *Effects of Radiation Damage on Polyimide Resistivity*, *Journal of Spacecraft and Rockets*, 2016.
65. Steckenreiter, T., et al., *Pyrolytic effects induced by energetic ions in polymers*, *Nuclear Instruments and Methods in Physics Research Section B: Beam Interactions with Materials and Atoms*, 1999, **151**(1-4), pp. 161-168.

## DISTRIBUTION LIST

DTIC/OCP 8725 John J. Kingman Rd, Suite 0944 Ft Belvoir, VA 22060-6218	1 cy
AFRL/RVIL Kirtland AFB, NM 87117-5776	2 cys
Official Record Copy AFRL/RVBXR/Ryan Hoffman	1 cy

This page is intentionally left blank.